

Probing the fluctuating magnetic field of Fe-triazole spin-crossover thin-layers with nitrogen-vacancy centers in diamond

Isabel Cardoso Barbosa,¹ Tim Hochdörffer,² Juliusz A. Wolny,² Dennis Lönard,¹
Stefan Johansson,¹ Jonas Gutsche,¹ Volker Schünemann,² and Artur Widera¹

¹*Department of Physics and State Research Center OPTIMAS,
University of Kaiserslautern-Landau, Erwin-Schrodinger-Str. 46, 67663 Kaiserslautern, Germany*

²*Department of Biophysics and Medical Physics, University of Kaiserslautern-Landau,
Erwin-Schrodinger-Str. 52, 67663 Kaiserslautern, Germany*

(Dated: November 25, 2024)

Fe^{II} spin-crossover (SCO) complexes are materials that change their magnetic properties upon temperature variation, exhibiting a thermal hysteresis. Particularly interesting for magnetic-memory applications are thin layers of SCO complexes, where practical magnetic probing techniques are required. While conventional magnetometry on SCO complexes employs cryogenic temperatures, nitrogen-vacancy (NV) centers are quantum magnetometers that can operate at room temperature with high spatial resolution and magnetic-field sensitivity. In this work, we apply thin layers of Fe-triazole SCO complexes directly onto a single-crystal diamond with shallow NV centers working as magnetic sensors and probe the fluctuating magnetic field. Using temperature-dependent NV-center T_1 measurements and a widefield technique, we find that the complexes are paramagnetic in the investigated temperature range from 20 °C to 80 °C. We quantitatively describe the T_1 time by a model considering the fluctuating magnetic field of the Fe^{II} ions. We see signatures of a local change of spin state in the T_1 relaxometry data, but structural changes in the SCO material dominate the local magnetic environment of the NV centers. Moreover, we conduct a Hahn echo to measure the T_2 time, which contrasts the findings of the T_1 times for the SCO complexes. We attribute this to different NV detection sensitivities towards Fe^{II} and Fe^{III} of the protocols. Our results on the magnetic properties of SCO materials highlight the capabilities of the NV center as a susceptible sensor for fluctuating magnetic fields. At the same time, a spin switching of the complexes cannot be observed due to the systematic challenges when working on nanometer distances to the SCO thin layers.

I. INTRODUCTION

NV centers in diamonds provide a spin-1 system susceptible to noise originating from fluctuating magnetic fields, influencing the NV centers' longitudinal relaxation time T_1 and the dephasing time T_2 [1–3]. Relaxometry is an established method of measuring the NV centers' T_1 time to detect high-frequency fluctuating magnetic fields from paramagnetic ions or molecules [1, 4]. The effect of Gd^{III} ions in aqueous solutions has been studied [5], and from relaxation measurements, the concentration of Gd^{III} ions has been determined [2]. In addition, this method has been shown to detect changes in the pH in aqueous solutions [6, 7] or to follow the process of chemical reactions [8, 9]. In the context of biological applications, relaxometry has been used to examine biomolecules of Fe^{III}, such as ferritin [3, 10], methemoglobin [11], and cytochrome C [12]. Also, the paramagnetic Fe^{II} ion in hemoglobin has been shown to reduce the NV centers' T_1 time [13]. Complementary to the T_1 time, the T_2 time of NV centers is influenced by low-frequency magnetic noise in superparamagnets [3, 14] and paramagnets [2]. Another system exhibiting interesting magnetic properties are iron-based SCO complexes that can change their spin state upon changing the temperature [15]. In detail, Fe^{II} SCO complexes switch from a diamagnetic low-spin (LS) state of spin quantum number $S = 0$ to a paramagnetic high-spin (HS) state of $S = 2$ with a thermal hysteresis

[16, 17]. For the application of memory devices, thin-layer samples of SCO complexes are especially of interest [18]. The magnetic properties of these complexes are usually examined using a Superconducting Quantum Interference Device (SQUID) [19], which operates at cryogenic temperatures [20, 21]. Recent emerging magnetometers are based on diamond NV centers, which allow the detection of static, alternating, and fluctuating magnetic fields with high sensitivity and spatial resolution at room temperature [22, 23]. The capabilities of NV centers in combination with complexes that switch their magnetic properties have recently been demonstrated for SCO nanorods [24] and SCO metal-organic frameworks [25] using optically detected magnetic resonance (ODMR).

This work employs a shallow NV layer in diamond to probe two Fe-triazole SCO complexes in thin-layer form, see Fig. 1(a). The complexes we investigate here are [Fe(Htrz)₂(trz)](BF₄), termed **SCO I**, and [Fe(atrz)₃](CH₃SO₃)_{4/3}(SO₄)_{1/3}, termed **SCO II** (Htrz = 1,2,4-4H-triazole, trz = 1,2,4-triazolate, atrz = 4-amino-1,2,4-triazole). These 1D-polymeric complexes exhibit spin-switching temperatures above room temperature [16, 18, 26, 27]. We use temperature-dependent NV-center relaxometry of the sequence depicted in Fig. 1(b) to investigate the fluctuating magnetic field originating from complexes **SCO I** and **SCO II** with spatial resolution. In comparison to the clean diamond, we observe a decrease of the NV-center T_1 time with SCO complexes

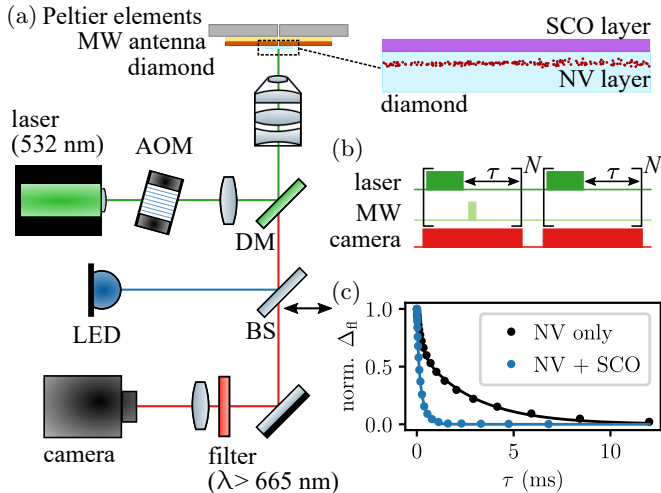


FIG. 1. Schematics of T_1 measurements in widefield configuration. (a) Microscope setup. A laser beam of wavelength 532 nm is pulsed by an acousto-optic modulator (AOM) and focused on the objective’s back focal plane to homogeneously illuminate a large section of the NV diamond sample. NV fluorescence is filtered by a 550-nm dichroic mirror (DM) and a 665-nm longpass filter and focused onto a camera. For orientation on the sample, a beam splitter (BS) can be moved into the beam path to illuminate the sample with light from a light-emitting diode (LED). The diamond sample has shallow NV centers implanted a few nm beneath its surface. SCO samples are directly drop-cast on the diamond. A microwave (MW) antenna guides MW pulses to the NV centers. The sample’s temperature is regulated with Peltier elements. (b) Pulsed sequence used for relaxometry measurements. (c) T_1 decays for the NV centers in the clean diamond ($T_1' = 2.80(12)$ ms) and an example with SCO complexes applied (**SCO I**, $T_1 = 0.27(1)$ ms). Solid lines are biexponential fit curves to the data points described in the main text.

applied on the diamond, see Fig. 1(c). Modeling the HS SCO layer on the diamond, we derive an estimated T_1 time for an NV center and compare the calculation to our experimental results. We compare the results for the T_1 times at different temperatures to the spin state of the SCO complexes we obtain with conventional Raman spectroscopy. In addition to that, we probe **SCO II** with a Hahn-echo measurement to obtain T_2 times of the NV centers close to the SCO layer. Since the T_1 time of the NV centers itself exhibits a temperature dependence [28, 29], we analyze the T_1 times for the NV-SCO samples at the same temperature in the heating and cooling branches of the hystereses.

II. SAMPLE PREPARATION

A. Diamond sample preparation

An ELSC (Single Crystal Electronic)-grade diamond chip of size $2 \times 2 \times 0.5$ mm³ from Element Six Technologies was irradiated with $^{14}\text{N}^+$ at an energy of 6 keV and

a dose of 4×10^{13} cm⁻² at an angle of 7°. Using a simulation [30], we estimate the depth of the NV layer to be $\bar{d} = 9.3$ nm of width $\sigma = 3.6$ nm in a Gaussian distribution. The diamond was then annealed in vacuum ($<7.8 \times 10^{-7}$ mbar), and the temperature was successively held at 400 °C (4 h) and 800 °C (2 h) [31, 32] to enhance the yield of NV centers. Afterward, the diamond chip was treated in a tri-acid solution (equal ratios of sulfuric acid (96%), perchloric acid (70%), and nitric acid (65%)) and heated to 500 °C (1 h) [31, 32] for diamond surface oxidation. Finally, the diamond was cleaned in acetone and isopropyl alcohol.

We perform T_1 measurements with the clean diamond chip or with SCO complexes directly cast on the diamond chip. To change the SCO sample on the diamond, SCO samples are removed from the diamond chip with alcohol/water solutions in an ultrasonic bath. We observe a recovery of the T_1 time from short T_1 times with the SCO complexes applied to long T_1 times after the cleaning process. Without any SCO complexes applied, we determine $T_1' = 2.80(12)$ ms. For a study on the temperature dependence of the T_1 time in our sample, see Supporting Information.

B. SCO synthesis

SCO I was synthesized according to the method described in Ref. [26]. **SCO II** was synthesized in a similar way, using a 2:1 mixture of $\text{Fe}(\text{CH}_3\text{SO}_3)_2 \cdot 7\text{H}_2\text{O}$ and $\text{FeSO}_4 \cdot 7\text{H}_2\text{O}$. The thin films were prepared as described below, similar to the method described in Ref. [18].

C. SCO application on diamond

We dissolved the SCO complexes **SCO I** and **SCO II** in water/alcohol solutions and added ascorbic acid to all solutions to prevent the SCO compounds from oxidizing. This resulted in colorless and transparent solutions.

SCO I

We dissolved 45 mg of compound **SCO I** in 4 mL water and 1 mL ethanol. We drop-cast ≈ 1 μL on the diamond chip and removed the solvent on a hot plate at ≈ 80 °C. This resulted in an amount of $n \approx 0.026$ μmol of SCO material on the diamond chip. The LS state of the SCO complexes was prepared by letting the sample cool down to room temperature.

Since the temperature for reaching the complexes’ HS state (110 °C) lay beyond the capabilities of our sample holder (max. 80 °C) for NV measurements, we applied external heating to the SCO-diamond sample. We first heated the sample holder to its maximum temperature and then put the sample on a hot plate to reach 115 °C. Next, we removed the external hot plate and held the

temperature at 80 °C to stay on the cooling branch of the hysteresis.

SCO II

Two similar solutions of complex **SCO II** were used for the measurements in this paper. We prepared solution 1 by adding 64 mg of **SCO II** to 5 mL ethanol and 2 mL water. For sample 1, we drop-cast $\approx 1 \mu\text{L}$ of solution 1 on the diamond chip. We removed the solvent on a hot plate at $\approx 60^\circ\text{C}$, which resulted in an amount of SCO material applied of $n \approx 0.020 \mu\text{mol}$. Solution 2 was prepared by dissolving 40 mg of **SCO II** in 5 mL water and 2 mL methanol. For sample 2, we drop-cast $\approx 3 \mu\text{L}$ of solution 2 on the diamond chip. This was done by application of drops of volume $\approx 1 \mu\text{L}$, removing the solvent, and repeating the process. The solvent was removed on a hot plate at $\approx 60^\circ\text{C}$. This process resulted in an amount of SCO material applied of $n \approx 0.037 \mu\text{mol}$.

To transfer samples of **SCO II** to the LS state, the colorless samples were cooled to -20°C for 15 min to 20 min. This resulted in a color change of the thin-layer samples from colorless to purple, indicating that the sample switched to the LS state [17].

D. Raman spectroscopy

We recorded Raman spectra of the SCO thin-layer samples on the diamond substrate. Raman experiments were performed with a Senterra[©] Raman Microscope (Bruker) using an excitation wavelength of 532 nm, at a laser power of 2 mW. The NV diamonds which were coated with the SCO materials were positioned inside a minicyostat (Linkam[©] stage FTIR600) and measurements were conducted in the temperature range of 290 K to 400 K. Local heating due to laser illumination is estimated to be $\approx 10\text{K}$ at the irradiated sample spot (diameter $< 2 \mu\text{m}$ to $3 \mu\text{m}$). Successive cycles of the SCO transition were investigated by cooling the NV diamonds to low temperatures within a liquid N_2 atmosphere or cooling to -20°C in the cooler between cycles.

III. NV-SENSING METHODS

A. T_1 measurements

We measure the NV centers' T_1 time in a microscope setup, as shown in Fig. 1(a). The NV centers are excited with a 532-nm laser of power of $\approx 80\text{mW}$. Laser pulses are created with an acousto-optic modulator (AOM). The laser light is focused onto the objective's (Nikon MRH08430, $40\times/0.60$) back focal plane to illuminate a large area of the NV layer in the diamond chip of $\approx 140 \mu\text{m}$ diameter. Using a 550-nm dichroic longpass, the NV fluorescence is filtered. Additionally,

we specifically filter the NV^- fluorescence using a 665-nm longpass filter. The NV fluorescence is detected with an electron-multiplying charge coupled device (EM-CCD) camera. For orientation on the sample before measurements, light from a white-light LED (light-emitting diode) can be guided through the objective with a removable 50:50 beam splitter and illuminate the sample homogeneously. The diamond chip is mounted in a temperature-controlled sample holder, which allows us to perform measurements between 20°C and $\approx 80^\circ\text{C}$. To drive transitions between the NV centers' spin states m_s , a microwave (MW) antenna is mounted directly above the NV diamond chip. We fabricated the antenna according to Ref. [33]. The diamond chip is oriented with its NV layer pointing towards the MW antenna to ensure high MW powers at the position of the NV-center layer. We employ Peltier elements to regulate the sample's temperature and a thermistor to read the temperature.

We perform relaxometry experiments without an external magnetic field to probe NV centers of all orientations at once, as previously reported in Refs. [2, 34], since we expect an equal influence of the paramagnetic Fe^{II} ions independent of the NV-center orientation. The pulsed sequence consists of laser pulses of $50 \mu\text{s}$ duration for NV-center spin polarization and readout, separated by a variable relaxation time τ , see Fig. 1(b). The pulses are repeated N times ($N \approx 2000$), during which the camera is exposed. In the first part of the measurement, an MW pulse transfers the NV centers from their spin ground state to an excited spin state. It follows $\approx 1 \mu\text{s}$ after the laser pulse and lies within τ . The sequence is repeated without the MW pulse being applied, and the camera is exposed again. For data acquisition, 40 exposures are accumulated for the sequence to one image with and without the MW pulse applied alternatingly for the same value of τ . The entire sequence is repeated 10 times. The T_1 signal is obtained by forming the difference between the two images for every value of τ , yielding the fluorescence difference [2, 28]. During the data evaluation, $10 \times 10 \text{px}^2$, corresponding to $2 \times 2 \mu\text{m}^2$ on the diamond surface, are binned together. This resolution of $2 \mu\text{m}$ is in the order of the expected resolution for our setup [35] and is sufficient for the investigations on a thin-layer sample. A mean fluorescence-difference decay $\Delta_{\text{fl}}(\tau)$ is calculated for every binned pixel. We normalize each $\Delta_{\text{fl}}(\tau)$ to its maximum and fit a function of type

$$\Delta_{\text{fl}}(\tau) = A \exp(-\tau/T_{1,1}) + B \exp(-\tau/T_{1,2}) \quad (1)$$

for every binned pixel. As pointed out in previous works, this biexponential T_1 decay is commonly observed in NV centers close to the diamond surface [34, 36]. Consistent with previous studies [2, 8, 34, 36], all T_1 times mentioned in this paper refer to the longer T_1 component found in the biexponential fit. The shorter T_1 component is attributed to cross-relaxation effects between NV centers of small distance to each other and NV centers very close to the diamond surface [2, 34]. We observe a similar influence of the SCO complexes on the shorter T_1

component. Examples for T_1 curves for the NV centers in the clean diamond and with a layer of SCO complexes applied on the diamond are shown in Fig. 1(c). Due to an inhomogeneity in the laser illumination of the sample caused by the Gaussian intensity distribution of the laser beam or interference patterns, the fluorescence intensity is not homogeneously distributed over the rectangular camera sensor. As a measure of the signal quality, we take the fluorescence contrast per binned pixel. We define the fluorescence contrast as the maximum $\Delta_{\text{fl}}(\tau)$ for each binned pixel and read out the maximum contrast for each T_1 map. In all position-resolved data sets shown below, we display regions of the T_1 map with a fluorescence contrast within the $1/e^2$ amplitude, while data with a contrast below the $1/e^2$ contrast is omitted. We provide the statistical fit errors ΔT_1 for each T_1 map presented in the Supporting Information.

We perform widefield ODMR spectroscopy to determine the NV centers' spin transition frequency for each temperature. Without an external magnetic field, the two excited m_s states $m_s = \pm 1$ of all NV centers are degenerate, respectively, and we excite all NV centers with an MW pulse at frequencies of ≈ 2866 GHz. To determine the duration of the MW pulse for T_1 measurements, we perform Rabi oscillations and choose the MW pulse duration yielding the highest fluorescence contrast. The MW pulse durations are in the order of 40 ns.

B. T_2 measurements

We measure the T_2 decoherence time with a Hahn-echo sequence [1, 22, 37]. For this, we use the same setup as depicted in Fig. 1(a) and a sequence similar to the relaxation sequence. The pulsed sequence consists of a laser pulse of 20 μs duration, followed by MW pulses $\frac{\pi}{2}$ - π - $\frac{\pi}{2}$, which are separated by waiting times $\frac{\tau}{2}$. During each exposure, the sequence is repeated $N = 5000$ times. We accumulate 30 exposures for one picture with and without the MW pulses applied for each value of τ and repeat the entire sequence 15 times. Again, we bin 10×10 px² in the data evaluation. We calculate the quotient of the fluorescence signals with and without the MW pulses for each binned pixel and fit a function of type $A \exp(-\tau/T_2) + c$ to the obtained relative fluorescence as a function of τ to extract the T_2 time for each binned pixel. In the Supporting Information, we provide the statistical fit errors ΔT_2 for each T_2 map shown in the main text. We omit pixels with fit results of $R^2 < 0.95$ in the T_2 maps. We perform the Hahn echo in an external magnetic field in the order of 11 mT generated by a permanent magnet to split the NV-center spin resonances. This way, we can probe NV centers specifically with MW pulses of duration π and $\pi/2$ in the Hahn-echo sequence at an MW frequency of ≈ 2813 MHz. The duration of the π - and $\pi/2$ -MW pulses are derived from Rabi oscillations.

IV. RESULTS AND DISCUSSION

A. Estimation of the effect of the paramagnetic HS Fe^{II} ions on the NV centers' T_1 time

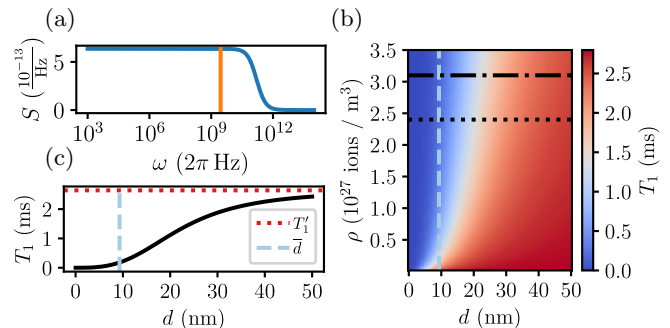


FIG. 2. (a) Spectral density $S(\omega)$, calculated for Fe^{II} ions (blue line). The NV-center spin-transition frequency at $\omega_0 \approx 2\pi \times 2.87$ GHz is marked (orange line). (b) Calculated values of T_1 as a function of the ion density ρ and the distance d of the NV centers to the diamond surface. The mean distance \bar{d} is marked as a blue dashed line. The value of $\rho_I = 3.1 \times 10^{27}$ ions/m³ is marked as a black dash-dotted line, the value of $\rho_{II} = 2.4 \times 10^{27}$ ions/m³ is marked as a black dotted line. (c) Calculated values for T_1 for $\rho = \rho_I$ as a function of d . The T_1 time for the NV centers without any SCO complexes, T_1' , is marked as a red dashed line. With $d = \bar{d}$ (blue dashed line), we expect a significant reduction of the T_1 time to 0.18 ms.

Before presenting the results of the T_1 measurements of NV centers with the SCO complexes in proximity, we mathematically estimate the influence of a layer of paramagnetic HS Fe^{II} ions on the NV centers' T_1 time. The spectral density of the fluctuating magnetic field of the Fe^{II} ions determines their influence on the NV centers' T_1 time. It is calculated by [10, 38]

$$S(\omega) = \frac{2}{\pi} \frac{\tau_c}{1 + \omega^2 \tau_c^2}, \quad (2)$$

where τ_c is the electron correlation time of Fe^{II}. We calculate the ions' spectral density with $\tau_c = 1 \times 10^{-12}$ s [39–42] and obtain a spectral density that spreads over a wide range of frequencies, see Fig. 2(a). Since the spectral density of Fe^{II} overlaps with the NV-center spin-transition frequency at $\omega_0 \approx 2\pi \times 2.87$ GHz, we expect an influence on the NV centers' T_1 time due to the ions' fluctuating magnetic field. The resulting T_1 time of the NV centers can be split into a sum of rates

$$\frac{1}{T_1} = \frac{1}{T_1'} + \frac{1}{T_1^{\text{SCO}}}, \quad (3)$$

where T_1' is the T_1 time of the NV centers in the diamond without any SCO complexes applied [2, 43, 44]. We calculate T_1^{SCO} by

$$\frac{1}{T_1^{\text{SCO}}} = 3\gamma_e^2 B_{\perp}^2 \frac{\tau_c}{1 + \omega_0^2 \tau_c^2}, \quad (4)$$

where B_{\perp}^2 describes the magnetic field variance of the Fe^{II} ions perpendicular to the NV-center quantization axis [2, 43, 44]. Approximating the angle α between the NV-center spin and the Fe^{II} ions to be 54.75° in our (100) surface oriented diamond (see Supporting Information), we calculate the transverse magnetic field variance by

$$B_{\perp}^2 = \rho \left(\frac{\mu_0 \gamma_e \hbar}{4\pi} \right)^2 \frac{S(S+1)}{3} (2 + 3 \sin^2 \alpha) \frac{\pi}{6d^3}. \quad (5)$$

Here, ρ is the Fe^{II} ion density, μ_0 is the vacuum permeability, γ_e is the gyromagnetic ratio of the electron, \hbar is the reduced Planck's constant, and S is the total spin quantum number of the Fe^{II} spin. Since we assume the SCO layer to be directly on the diamond surface, d , the depth of the NV-center layer, is also the distance of the NV spin to the Fe^{II} layer. In the geometry described here, B_{\perp}^2 exhibits a $1/d^3$ dependence, as previously pointed out in Refs. [2, 34].

Using Eq. 4, we calculate the T_1 time as a function of the distance d of the NV centers to the diamond surface and the Fe^{II} ion density ρ , see also Supporting Information. Figure 2(b) shows the result of this calculation. Starting with $T_1' = 2.8$ ms, the T_1 time can drop by several orders of magnitude, depending on d and ρ . The estimated mean depth of the NV layer $\bar{d} = 9.3$ nm is marked as a dashed blue line in Fig. 2(b). Further, we estimate ρ from crystal structures of SCO complexes of the constitution or a similar constitution to **SCO I** [45] and **SCO II** [46]. From the given unit-cell volumes, we obtain $\rho_{\text{I}} = 3.1 \times 10^{27}$ ions/m³ and $\rho_{\text{II}} = 2.4 \times 10^{27}$ ions/m³ for **SCO I** and **SCO II**, respectively, which are marked in Fig. 2(b) as horizontal lines. We consider these values of ρ as the maximum possible ion densities since the crystal structures contain densely packed iron ions, ligands, and counter ions. However, in our case, we apply thin-layer samples that might exhibit a lower ion density than the crystal structures due to a different crystallization process and finite chain lengths of the polymeric structures. The T_1 time calculated as a function of d for ρ_{I} is presented in Fig. 2(c). From our calculations, we obtain reductions of $T_1' = 2.80$ ms to $T_1 = 0.18$ ms for **SCO I** and $T_1 = 0.23$ ms for **SCO II** at $d = \bar{d} = 9.3$ nm. This corresponds to effective magnetic-field values of $\sqrt{B_{\perp, \text{I}}^2} = 0.24$ mT and $\sqrt{B_{\perp, \text{II}}^2} = 0.21$ mT at the NV position.

B. T_1 measurements on **SCO I**

We apply a thin-layer sample of **SCO I** on the diamond chip. Investigation of the surface under LED illumination shows visible structures in the thin layer as shown in Fig. 3(a), which was recorded after several cycles of heating and cooling of the sample. A T_1 measurement at room temperature of the same section is shown in Fig. 3(b). We see an overall reduction in the T_1 time from $T_1' = 2.80(12)$ ms to lower T_1 times, with

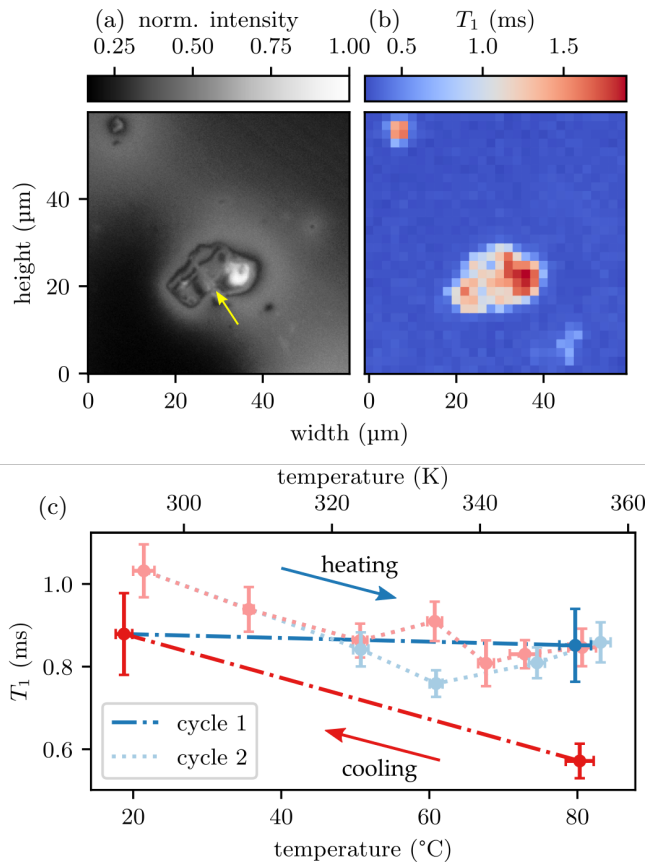


FIG. 3. T_1 measurements for the thin-layer sample of **SCO I**. (a) LED image of the sample **SCO I** drop-cast on the diamond chip after several heating and cooling cycles. Within the homogeneous thin layer, characteristic structures are visible. The yellow arrow indicates the position investigated in (c) for different temperatures. (b) T_1 map of the same region, recorded at room temperature with widefield relaxometry. The spatial distribution of the T_1 times coincides with the structures in the LED image. (c) T_1 values as a function of the temperature, recorded for the position marked in the LED image with confocal microscopy for two subsequent heating and cooling cycles. The red arrow indicates the cooling branch, in which the sample was heated to 115°C , cooled to 80°C , and measurements recorded. The temperatures were then swept to room temperature, and the sample was again heated to 80°C (heating branch), and measurements were recorded. The errors of T_1 are the statistical fit errors. The errors of the temperatures are derived from statistical fit errors and the difference between the calculated temperature by ODMR spectroscopy and the temperature determined by the temperature sensor, see Supporting Information.

a maximum of $T_1 = 1.89(8)$ ms. From the comparison of Figs. 3(a) and (b), it becomes clear that the visible structures in Fig. 3(a) correspond to regions of higher T_1 times, whereas sections of homogeneous appearance exhibit shorter T_1 times. Therefore, we conclude that the structures consist of SCO material, which has lifted off the diamond chip during heating and cooling, resulting in

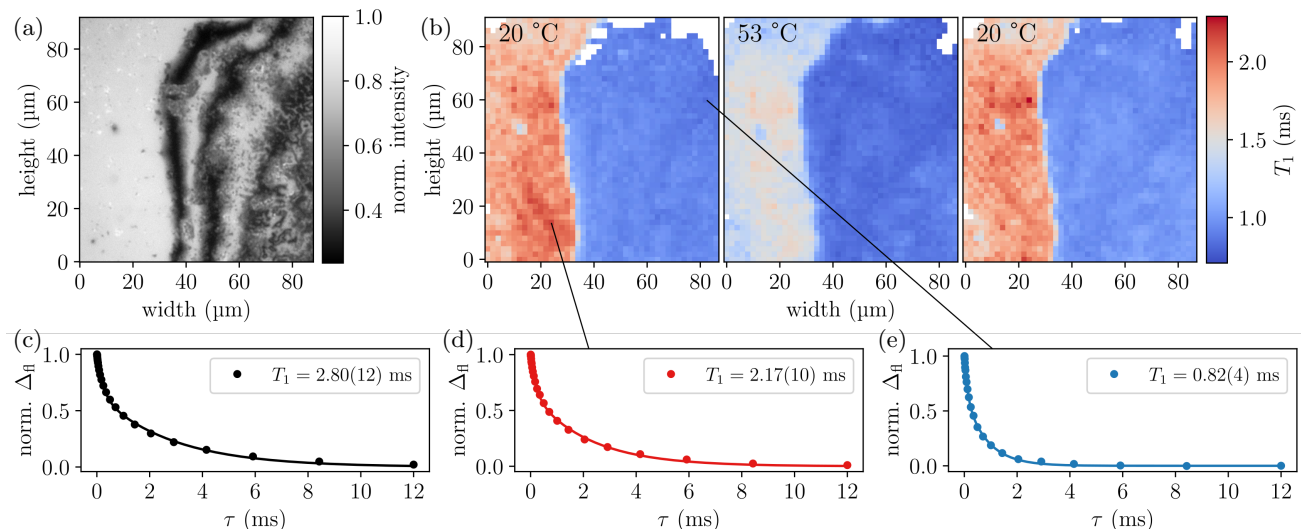


FIG. 4. T_1 measurements for the thin-layer sample of **SCO II**, sample 1. (a) LED image of the structure visible on the thin-layer sample. (b) Spatially-resolved T_1 measurements for the same area as shown in (a) for different temperatures. The measurements were recorded in the order of appearance (left to right). After cooling the sample to -20°C , we record the T_1 map at $20(1)^\circ\text{C}$ in the heating branch. Then, the T_1 times are measured at $53(2)^\circ\text{C}$. Lastly, the sample is cooled back to $20(1)^\circ\text{C}$ to record the T_1 times in the cooling branch. Pixels of low fluorescence contrast are displayed in white (no T_1 time given). (c) T_1 curve (norm. Δ_H as a function of τ) for the NV centers in the clean diamond (no SCO complexes applied) at room temperature. (d) T_1 curve for the maximum T_1 at $20(1)^\circ\text{C}$. (e) T_1 curve for the minimum T_1 at $20(1)^\circ\text{C}$. The solid lines in (c), (d), and (e) are fit curves as described in the methods section. The black lines indicate the positions in (b) at which the respective T_1 times are found.

a more considerable distance d of the NV centers to the SCO sample. According to our calculations, this change in T_1 could be caused by lifting the sample by ≈ 20 nm. Likewise, less SCO material at these specific positions or a combination of the two reasons might explain the longer T_1 times measured in these regions. The shortest T_1 time we measure in Fig. 3(b) is $T_1 = 0.27(1)$ ms, which reduces T_1' by one order of magnitude. This measured T_1 time corresponds to an effective magnetic-field value of $\sqrt{B_1^2} = 0.189(5)$ mT, the uncertainty is derived from error propagation of the T_1 -time errors. The measured T_1 time lies in the same order of magnitude as calculated in our model, $T_1 = 0.18$ ms, which, however, assumes all Fe^{II} ions to be in their HS state. At room temperature, the complex is in its LS state and should exhibit diamagnetism [16, 17], which is not known to shorten the NV centers' T_1 time [36]. However, from our T_1 measurements, we conclude that most of the complexes are paramagnetic at room temperature. Our findings agree with measurements on similar SCO systems in Refs. [24, 25], where paramagnetism of the LS complexes was observed with ODMR spectroscopy. One explanation for the paramagnetism at room temperature is that terminal Fe^{II} ions at the ends of the polymeric chains are most likely in the HS state, independent of the temperature [47]. Crystal defects between the polymeric chains additionally reduce the number of switchable Fe ions in the SCO material [48, 49]. A relaxometry study on single crystals of these SCO complexes could gain insight into the chain-length

dependent ratio of Fe^{II} ions that undergo a spin transition upon temperature variation. Likewise, Fe ions on the surface or on the SCO-diamond interface could favor a HS state because of partial coordination [25, 50]. Another reason for temperature-independent paramagnetism are Fe^{III} impurities in the SCO material, which have a similar correlation time as Fe^{II} [41], and could be caused by oxidation of the SCO material [24, 25]. Since the T_1 time is already reduced close to a minimum value at the complexes' LS state, we expect no further decrease in the T_1 time after heating the sample.

We probe the sample at different temperatures at a specific position as indicated with a yellow arrow in Fig. 3(a) in two subsequent cycles of the hysteresis and record the T_1 time at different temperatures, see Fig. 3(c). These experiments were performed with a confocal configuration, see Supporting Information for a detailed description. We first transfer the SCO sample into its HS state by externally heating it to 115°C . We then let the sample cool down to 80°C and record the T_1 time in the cooling branch (red arrow in Fig. 3(c)). After this, we let the sample cool down to room temperature and record the T_1 time at the LS state of the SCO. To measure the T_1 time in the heating branch, we then heat the sample again (blue arrow in Fig. 3(c)). Raman spectroscopy suggests that the sample is in its LS state at 80°C in the heating and cooling branch. It is important to note that the T_1 time of NV centers is known to be temperature dependent [28, 29], see also Supporting In-

formation. Therefore, we compare the T_1 times pairwise in heating and cooling branches at the same temperature. The T_1 times we measure at 80 °C differ significantly in the first cycle of $T_1 = 0.57(4)$ ms in the cooling branch to $T_1 = 0.85(9)$ ms in the heating branch, see Fig. 3(c). In addition to that, the change in $T_1 = 0.9(1)$ ms at room temperature to the shorter T_1 time of $T_1 = 0.57(4)$ ms at 80 °C would be beyond the expected NV temperature effects of the T_1 time (≈ 0.72 ms from Eq. 3). We interpret this as a signature of a local change in the spin state of the SCO thin-layer sample. However, repeating our measurements, the T_1 times at 80 °C coincide in the second cycle, while the T_1 times measured at 60 °C differ from one another. Structural changes in the SCO thin-layer sample most likely cause the changes in the T_1 times in the branches. Since the SCO sample is in its LS state at 80 °C in both branches, the discrepancy of the T_1 times in the cycles are presumably not caused by a change in the complexes' spin state. We observe a visible structural change in the sample during heating and cooling, see Supporting Information. It is known that SCO complexes change their volume when undergoing a spin transition [45]. Therefore, we assume that fractures in the SCO sample caused by repeated heating and cooling change the local environment of the NV centers and, with it, the T_1 time we measure. We conclude that structural changes in the sample and the accompanying changes in the local environment of the NV centers are prominent and dominate the measured T_1 times. Indications of a local spin change of the SCO complexes are overshadowed by this effect.

C. T_1 measurements on SCO II

Since the spin-switching temperature for **SCO I** lies beyond the temperatures at which we can record measurements, we apply another SCO compound to our NV diamond, **SCO II**, which switches its spin state at significantly lower temperatures. From Raman spectroscopy, we find that the complex is 62 % in its HS state at room temperature. In contrast, above 35 °C, the complexes switch to 84 % HS, where they remain after cooling to room temperature, see Supporting Information. According to our model, this change in the density of Fe^{II} ions in the HS state should be accompanied by a significant decrease in the T_1 time, see below. We investigate two samples of **SCO II**, which differ by the amount of SCO material applied, see Sec. II.

In the first sample, a comparable amount of **SCO II** is applied on the NV-diamond chip as we presented previously for **SCO I**. An LED image and T_1 data for different temperatures can be seen in Fig. 4(a). In the image, a dark shade is visible on the right half of the image. We interpret this as a higher density of SCO material on the diamond sample. Recording the T_1 times in this specific region, we find that the T_1 time is reduced compared to T_1' in the entire area, see Fig. 4(b) in comparison to

Fig. 4(c). We find a maximum of $T_1 = 2.17(10)$ ms, see Fig. 4(d), and a minimum of $T_1 = 0.82(4)$ ms at 20 °C, see Fig. 4(e), indicating a paramagnetic sample. We also observe that the T_1 time is especially short in the right half of the observed area, while it is up to an order of magnitude longer on the left half. This coincides with the intensity distribution in the LED image and underlines our notion that a higher density of SCO material is present in the dark-shaded areas of the image, leading to a reduced T_1 time. We heat the complexes beyond the spin transition temperature and perform T_1 measurements again at 53 °C. The contrast in T_1 times between the left and right side of the map persists, however, it is diminished due to temperature effects in the diamond, influencing the T_1 time of the NV centers, see Fig. 4(b). We find a reduction to a maximum of $T_1 = 1.69(7)$ ms and a minimum of $T_1 = 0.71(4)$ ms, which is in the order of what we expect from the temperature dependence of the T_1 time for the bare diamond, see Supporting Information. To separate temperature effects and effects due to the spin switching of the SCO material, we cool the sample back to 20 °C and repeat the T_1 measurements in the cooling branch. We find that the T_1 times coincide with the T_1 times measured previously in the heating branch at 20 °C, with a maximum of $T_1 = 2.29(10)$ ms and a minimum of $T_1 = 0.82(4)$ ms. Calculated from our model, a change of the HS-Fe density from 62 % to 84 % should have reduced the T_1 minimum to $T_1 = 0.66$ ms, which we do not observe. Temperature-independent paramagnetism of the SCO samples prevail and overshadow the effects on the T_1 time of the spin transition. We observe a similar behavior in a second cycle, see Supporting Information.

To test the effect of a thicker SCO layer on the NV centers' T_1 time, we repeat the measurements on a second sample of **SCO II**. Here, we apply approximately twice the amount of SCO material on the diamond chip compared to sample 1. The results for this sample can be seen in Fig. 5 for two subsequent cycles. Again, we choose a particular spot of the sample with visible characteristics in the thin layer. The structure investigated is rectangular, surrounded by a circular pattern, see Fig. 5(a). We find that the T_1 map at 20 °C again shows similar spatial characteristics as the LED image of the area. At room temperature, we find that the T_1 time in the observed area is approximately the same as T_1' , with a maximum of $T_1 = 2.86(12)$ ms, see Fig. 5(b). In contrast, the rectangular structure exhibits a notably shorter T_1 time than its surroundings, with a minimum of $T_1 = 1.86(9)$ ms. We heat the sample above the SCO spin-transition temperature to 40 °C and repeat the T_1 measurements, see the first row of Fig. 5(b). The T_1 time decreases overall, showing a maximum of $T_1 = 2.08(9)$ ms. The minimum T_1 time within the rectangular structure lies at $T_1 = 1.59(6)$ ms. The decrease in the T_1 time in this area is in the order of T_1 reduction expected due to temperature effects of the bare diamond. Separating T_1 temperature effects from possible SCO effects, we let the sample

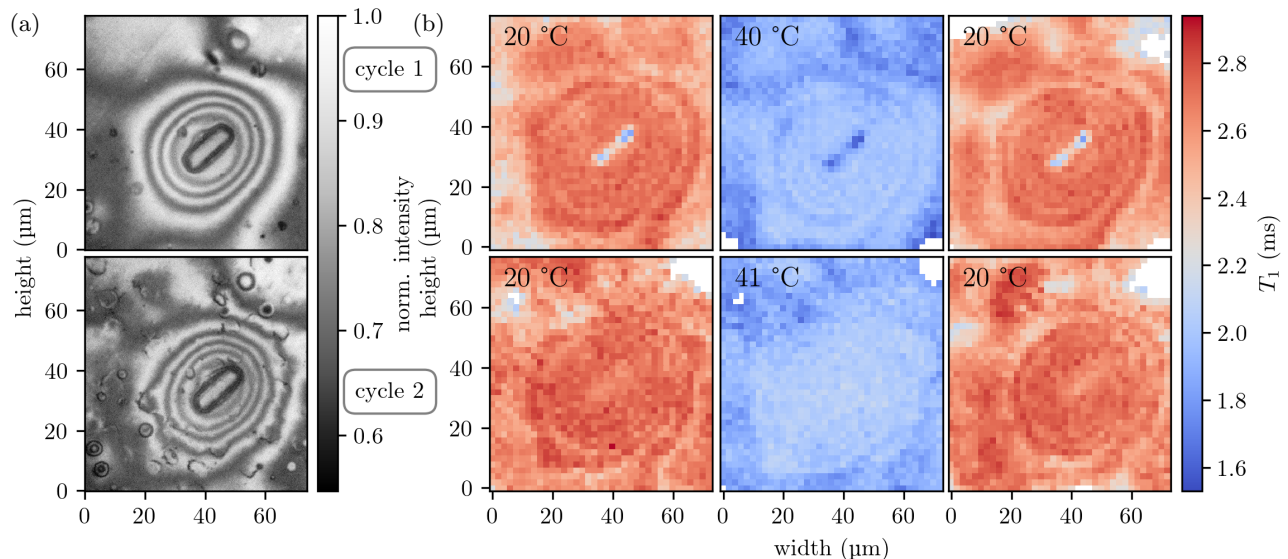


FIG. 5. T_1 measurements for the thin-layer sample 2 of **SCO II** for two subsequent heating and cooling cycles. The first row (second row) displays the data for the first cycle (second cycle). (a) LED image of the structure visible on the thin-layer sample at the beginning of the first and second cycles. Comparing the two images, heating and cooling the sample has caused cracks in the sample from the first to the second cycle. (b) Spatially-resolved T_1 measurements for the same area as shown in (a) for different temperatures for the first and second cycles. The measurements were recorded in the order of appearance (left to right). After cooling the sample to -20°C , we record the T_1 map at $20(1)^\circ\text{C}$ in the heating branch. Then, the T_1 times are measured at $40(2)^\circ\text{C}$ ($41(2)^\circ\text{C}$) for cycle 1 (cycle 2). Lastly, the sample is cooled back to $20(1)^\circ\text{C}$ to record the T_1 times in the cooling branch. While the rectangular structure in (a) exhibits a lower T_1 time than its surroundings in the first cycle, this T_1 contrast fades in the second cycle. Pixels of low fluorescence contrast are displayed in white (no T_1 time given).

cool down to room temperature and repeat the measurement. We find that the T_1 time is restored to its values in the heating branch with a maximum of $T_1 = 2.82(11)$ ms and a minimum of $T_1 = 1.81(8)$ ms, which lies within the rectangular structure. We probe the sample in a second cycle, see the second row of Fig. 5. After cooling the sample, the structure has visibly changed, see Fig. 5(a). Cracks have appeared, especially in the surroundings of the rectangular structure. We record the T_1 map for this area and find that the rectangular structure no longer exhibits a shorter T_1 time than its surroundings and find a mean $T_1 = 2.64(12)$ ms for the entire area at room temperature, which coincides with T_1' . At increased temperature, we obtain a mean $T_1 = 1.95(9)$ ms. Cooling back to room temperature, we measure $T_1 = 2.62(13)$ ms, where the errors denote the standard deviations. We assume that the SCO complexes of rectangular shape lifted off the diamond chip after the second cooling process, causing the T_1 time to increase in the second cycle. We observe no effect on the NV centers' T_1 time due to the spin switching of the SCO complexes. We note that in a second position on the same sample, we observe a similar behavior, see Supporting Information. These results underline that the method applied here is susceptible to small changes in the distance of the SCO complexes to the diamond surface. One reason for the overall higher T_1 time in this sample compared to the previous ones might be that the thicker SCO layer has poor contact with the

diamond chip and tends to detach from the substrate when cooling and heating, which results in a larger mean distance of the SCO layer to the NV layer. We observe that even thicker layers of the complexes chip off the diamond after heating or cooling completely, making T_1 measurements with thicker SCO layers inaccessible.

While the presented measurements show a spatial distribution of T_1 times that coincides with the visible structure of the SCO material, no spin switching of the SCO complexes can be demonstrated with our method. Compared to **SCO I**, which is in its LS state at the temperatures we probed, **SCO II** is mostly in its HS state. Nevertheless, the T_1 times we observe for **SCO II** are still in the same order of magnitude as for **SCO I**, although both complexes should exhibit different amounts of HS Fe^{II} ions. We conclude from this that paramagnetic centers within the SCO complexes in their LS state already dominate the result of the T_1 measurements, causing the method to be unable to detect additional changes in the spin state of the SCO complexes.

D. T_2 measurements on SCO II

While T_1 relaxometry is known to detect fluctuating magnetic fields in the GHz range, Hahn echoes are sensitive towards lower-frequency fluctuating magnetic fields in the MHz range [3]. To shift the detection window

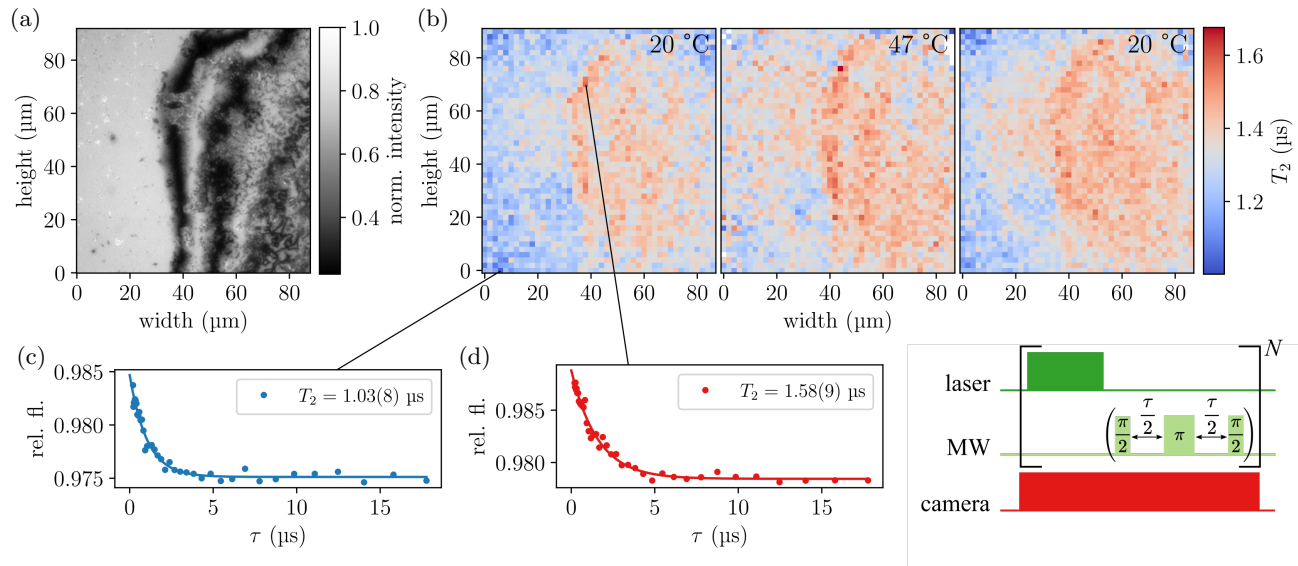


FIG. 6. T_2 measurement (Hahn echo) for the thin-layer sample 1 of **SCO II** in the third cooling and heating cycle. We use a measurement sequence as shown and described in the methods section. (a) LED image of the structure examined. (b) Spatially-resolved T_2 measurements for the same area as shown in (a) for different temperatures. The data was recorded in order of appearance (left to right). After cooling the sample to -20°C , we record the T_2 times at $20(1)^\circ\text{C}$ in the heating branch. Next, we heat the sample to $47(4)^\circ\text{C}$, repeat the measurement, and let it cool to $20(1)^\circ\text{C}$ to repeat the measurement in the cooling branch. (c) Relative fluorescence (rel. fl.) as a function of τ for the minimum T_2 at $20(1)^\circ\text{C}$. (d) Relative fluorescence as a function of τ for the maximum T_2 at $20(1)^\circ\text{C}$. The solid lines in (c) and (d) are fit curves as described in the methods section. The black lines indicate the positions at which the respective T_2 times are found.

to these lower frequencies, we perform a Hahn echo on **SCO II**, sample 1, at the same position as previously shown for T_1 relaxometry in Fig. 4 in a third cycle. We perform these experiments in an external magnetic field ($\approx 11\text{mT}$) to precisely control NV centers of one orientation in the diamond lattice with MW pulses and probe the NV centers with MW frequencies of $\approx 2813\text{MHz}$. Since the spectral density of the magnetic field of the Fe^{II} ions is distributed over a wide frequency range, see Fig. 2(a), the Hahn echo should be able to detect the fluctuating magnetic field arising from the paramagnetic SCO complexes. We show the measurement sequence and the results for different temperatures in Fig. 6. The LED image of the structure in Fig. 6(a) shows the same characteristics as previously presented in Fig. 4. We note that the measured T_2 times are three orders of magnitude lower than the T_1 times we measure, see Fig. 6(b). The spatial distribution of the T_2 times coincides with the structures we see in the LED image in Fig. 6(a). However, the areas of the different densities of SCO material are not as clearly separated by differences in T_2 as in the T_1 measurements. We conclude from this that the Hahn echo is less sensitive towards the fluctuating magnetic field of the paramagnets, which conforms with the observations made by Ref. [2]. In addition, we do not observe any changes in the T_2 times upon temperature variation. While the T_1 measurements in Fig. 4 show a reduced T_1 time in darker areas of the sample in comparison to brighter areas, we find that the opposite is the case for the T_2 time, see Fig. 6(b). We

find a minimum of $T_2 = 1.03(8)\mu\text{s}$ and a maximum of $T_2 = 1.58(9)\mu\text{s}$, see Figs. 6(c) and (d), at the indicated positions. In addition to that, we observe that the T_2 time in the right half of the area is slightly increased in comparison to the T_2 time of the NV centers without SCO complexes of $T_2' = 1.26(5)\mu\text{s}$, see Supporting Information. These contrasting results between T_1 and T_2 measurements might be caused by changes in the detection sensitivity of the NV center for Fe^{II} or Fe^{III} in the significantly different detection windows of the measurement sequences. Further investigations on this topic are necessary, which could involve tuning the T_1 detection window by application of an external magnetic field or implementation of more complex pulse sequences, such as CPMG (Carr-Purcell-Meiboom-Gill) sequences, which are known to show higher sensitivities towards the detection of paramagnetic noise than the Hahn echo [2]. In addition, the systematic influence of nanoscale distance changes between SCO layer and NV layer on T_1 and T_2 measurements can be studied to gain further insight into the fluctuating magnetic fields of Fe^{II} and Fe^{III} .

V. CONCLUSIONS

In this work, we probe the fluctuating magnetic field of SCO thin-layer samples with NV centers in diamond implanted at 9.3nm depth. For this, we perform spatially resolved NV-center relaxometry to quantify influences of

the paramagnetic Fe ions on the T_1 times at different temperatures. From our results, we conclude that paramagnetic centers dominate the results of the T_1 measurement for the LS complexes. We initially observe indications of a local change in the SCOs' spin state. However, the temperature variation causes structural changes in the thin-layer sample, affecting the T_1 time due to an altered sample-NV distance. These effects are so prominent that an additional change in the SCO complexes' spin state from LS to HS cannot be detected. These findings underline the high sensitivity of NV-center relaxometry for the detection of paramagnetic materials and the high susceptibility towards changes in the distance of the sample to the NV layer.

ACKNOWLEDGMENTS

We acknowledge support from the Nano Structuring Center (NSC) of the RPTU Kaiserslautern-Landau. This project was funded by the Deutsche Forschungsgemeinschaft (DFG, German Research Foundation)—Project-ID No. 454931666 in the initial stages and QUIP (Quanten-Initiative Rheinland-Pfalz). Further, I. C. B. thanks the Studienstiftung des deutschen Volkes. T. H., J. A. W., and V. S. acknowledge the support by the Deutsche Forschungsgemeinschaft (DFG) through CRC/TRR173, “Spin + X”, project A4. We thank O. Opaluch and E. Neu-Ruffing (RPTU Kaiserslautern), M. Schreck and W. Brückner (Augsburg University) for diamond ion implantation. Further, we thank O. Opaluch for the diamond sample preparation. We thank M. Weiler, Z. Zhang, N. Mathes, and F. Freire-Moschovitis for helpful discussions, and J. Witzernath for experimental support. We would like to express special gratitude to E. Neu-Ruffing and O. Opaluch, who have given us valuable experimental support during our work.

-
- [1] E. V. Levine, M. J. Turner, P. Kehayias, C. A. Hart, N. Langellier, R. Trubko, D. R. Glenn, R. R. Fu, and R. L. Walsworth, Principles and techniques of the quantum diamond microscope, *Nanophotonics* **8**, 1945 (2019).
- [2] S. Steinert, F. Ziem, L. T. Hall, A. Zappe, M. Schweikert, N. Götz, A. Aird, G. Balasubramanian, L. Hollenberg, and J. Wrachtrup, Magnetic spin imaging under ambient conditions with sub-cellular resolution, *Nat. Commun.* **4**, 1607 (2013).
- [3] E. Schäfer-Nolte, L. Schlipf, M. Ternes, F. Reinhard, K. Kern, and J. Wrachtrup, Tracking temperature-dependent relaxation times of ferritin nanomagnets with a wideband quantum spectrometer, *Phys. Rev. Lett.* **113**, 217204 (2014).
- [4] A. Mzyk, A. Sigaeva, and R. Schirhagl, Relaxometry with Nitrogen Vacancy (NV) Centers in Diamond, *Acc. Chem. Res.* **55**, 3572 (2022).
- [5] S. Iyer, C. Yao, O. Lazorik, P. Wang, G. Glenn, M. Mohs, Y. Shi, M. Mansour, E. Henriksen, K. Murch, S. Mukherji, and Chong, Optically-Trapped Nanodiamond-Relaxometry Detection of Nanomolar Paramagnetic Spins in Aqueous Environments, arXiv:2401.17372 [quant-ph].
- [6] T. Fujisaku, R. Tanabe, S. Onoda, R. Kubota, T. F. Segawa, F. T.-K. So, T. Ohshima, I. Hamachi, M. Shirakawa, and R. Igarashi, pH Nanosensor Using Electronic Spins in Diamond, *ACS Nano* **13**, 11726 (2019).
- [7] H. Cheng, Y. Luo, X. Luo, C. Xue, Y. Li, G. Liu, L. Chen, Z. Chen, and Y. Chen, All-fiber quantum relaxometry for biochemical sensing based on diamond NV centers, *Opt. Express* **32**, 29265 (2024).
- [8] F. Perona Martínez, A. C. Nusantara, M. Chipaux, S. K. Padamati, and R. Schirhagl, Nanodiamond Relaxometry-Based Detection of Free-Radical Species When Produced in Chemical Reactions in Biologically Relevant Conditions, *ACS Sens.* **5**, 3862 (2020).
- [9] R. Li, T. Vedelaar, A. Mzyk, A. Morita, S. K. Padamati, and R. Schirhagl, Following Polymer Degradation with Nanodiamond Magnetometry, *ACS Sens.* **7**, 123 (2022).
- [10] E. S. Grant, L. T. Hall, L. C. L. Hollenberg, G. McColl, and D. A. Simpson, Nonmonotonic Superparamagnetic Behavior of the Ferritin Iron Core Revealed via Quantum Spin Relaxometry, *ACS Nano* **17**, 372 (2023).
- [11] S. Lamichhane, E. C. Guevara, I. Fescenko, S.-H. Liou, R. Y. Lai, and A. Laraoui, Magnetic relaxometry of methemoglobin by widefield nitrogen-vacancy microscopy, *Appl. Phys. Lett.* **125**, 114002 (2024).
- [12] S. Lamichhane, R. Timalina, C. Schultz, I. Fescenko, K. Ambal, S.-H. Liou, R. Y. Lai, and A. Laraoui, Nitrogen-Vacancy Magnetic Relaxometry of Nanoclustered Cytochrome C Proteins, *Nano Lett.* **24**, 873 (2024).
- [13] F. Gorrini, R. Giri, C. E. Avalos, S. Tambalo, S. Mannucci, L. Basso, N. Bazzanella, C. Dorigoni, M. Cazzanelli, P. Marzola, A. Miotello, and A. Bifone, Fast and Sensitive Detection of Paramagnetic Species Using Coupled Charge and Spin Dynamics in Strongly Fluorescent Nanodiamonds, *ACS Appl. Mater. Interfaces* **11**, 24412 (2019).
- [14] D. Schmid-Lorch, T. Häberle, F. Reinhard, A. Zappe, M. Slota, L. Bogani, A. Finkler, and J. Wrachtrup, Relaxometry and Dephasing Imaging of Superparamagnetic Magnetite Nanoparticles Using a Single Qubit, *Nano Lett.* **15**, 4942 (2015).
- [15] P. Gütllich, Y. Garcia, and H. A. Goodwin, Spin crossover phenomena in Fe(II) complexes, *Chem. Soc. Rev.* **29**, 419 (2000).
- [16] O. Roubeau, Triazole-Based One-Dimensional Spin-Crossover Coordination Polymers, *Chem. Eur. J.* **18**, 15230 (2012).
- [17] S. Brooker, Spin crossover with thermal hysteresis: practicalities and lessons learnt, *Chem. Soc. Rev.* **44**, 2880 (2015).

- [18] T. Hochdörffer, J. A. Wolny, L. Scherthan, H. Auerbach, S. Sakshath, A. Omlor, S. Wolff, H.-C. Wille, I. Sergeev, and V. Schünemann, Preparation and characterization of spin crossover thin solid films, *Hyperfine Interact.* **240**, 116 (2019).
- [19] R. W. Hogue, S. Singh, and S. Brooker, Spin crossover in discrete polynuclear iron(II) complexes, *Chem. Soc. Rev.* **47**, 7303 (2018).
- [20] B. Bao, Y. Hua, R. Wang, and D. Li, Quantum-Based Magnetic Field Sensors for Biosensing, *Adv. Quantum Technol.* **6**, 2200146 (2023).
- [21] L. Bishop-Van Horn, Z. Cui, J. R. Kirtley, and K. A. Moler, Cryogen-free variable temperature scanning SQUID microscope, *Rev. Sci. Instrum.* **90**, 063705 (2019).
- [22] J. F. Barry, J. M. Schloss, E. Bauch, M. J. Turner, C. A. Hart, L. M. Pham, and R. L. Walsworth, Sensitivity optimization for NV-diamond magnetometry, *Rev. Mod. Phys.* **92**, 015004 (2020).
- [23] L. T. Hall, J. H. Cole, C. D. Hill, and L. C. L. Hollenberg, Sensing of fluctuating nanoscale magnetic fields using nitrogen-vacancy centers in diamond, *Phys. Rev. Lett.* **103**, 220802 (2009).
- [24] S. Lamichhane, K. A. McElveen, A. Erickson, I. Fescenko, S. Sun, R. Timalina, Y. Guo, S.-H. Liou, R. Y. Lai, and A. Laraoui, Nitrogen-Vacancy Magnetometry of Individual Fe-Triazole Spin Crossover Nanorods, *ACS Nano* **17**, 8694 (2023).
- [25] B. T. Flinn, G. A. Rance, W. J. Cull, I. Cardillo-Zallo, J. Pitcairn, M. J. Cliffe, M. W. Fay, A. J. Tyler, B. L. Weare, C. T. Stoppiello, E. S. Davies, M. L. Mather, and A. N. Khlobystov, Sensing the Spin State of Room-Temperature Switchable Cyanometallate Frameworks with Nitrogen-Vacancy Centers in Nanodiamonds, *ACS Nano* **18**, 7148 (2024).
- [26] J. Kroeber, J.-P. Audiere, R. Claude, E. Codjovi, O. Kahn, J. G. Haasnoot, F. Groliere, C. Jay, and A. Bousseksou, Spin Transitions and Thermal Hysteresis in the Molecular-Based Materials $[\text{Fe}(\text{Htrz})_2(\text{trz})](\text{BF}_4)$ and $[\text{Fe}(\text{Htrz})_3](\text{BF}_4)_2 \cdot \text{H}_2\text{O}$ (Htrz = 1,2,4-H-triazole; trz = 1,2,4-triazolato), *Chem. Mater.* **6**, 1404 (1994).
- [27] T. Hochdörffer, *Optical and deformation induced spin switching in SCO materials*, Berichte aus der Physik (Shaker Verlag, Düren, 2023) ISBN: 978-3-8440-8913-4.
- [28] A. Jarmola, V. M. Acosta, K. Jensen, S. Chemerisov, and D. Budker, Temperature- and magnetic-field-dependent longitudinal spin relaxation in nitrogen-vacancy ensembles in diamond, *Phys. Rev. Lett.* **108**, 197601 (2012).
- [29] A. Norambuena, E. Muñoz, H. T. Dinani, A. Jarmola, P. Maletinsky, D. Budker, and J. R. Maze, Spin-lattice relaxation of individual solid-state spins, *Phys. Rev. B* **97**, 094304 (2018).
- [30] J. F. Ziegler, M. D. Ziegler, and J. P. Biersack, SRIM (The Stopping and Range of Ions in Matter), Version SRIM-2013.00 (2012).
- [31] Y. Chu, N. P. de Leon, B. J. Shields, B. Hausmann, R. Evans, E. Togan, M. J. Burek, M. Markham, A. Stacey, A. S. Zibrov, A. Yacoby, D. J. Twitchen, M. Loncar, H. Park, P. Maletinsky, and M. D. Lukin, Coherent optical transitions in implanted nitrogen vacancy centers, *Nano Lett.* **14**, 1982 (2014).
- [32] P. Appel, E. Neu, M. Ganzhorn, A. Barfuss, M. Batzer, M. Gratz, A. Tschöpe, and P. Maletinsky, Fabrication of all diamond scanning probes for nanoscale magnetometry, *Rev. Sci. Instrum.* **87**, 063703 (2016).
- [33] K. Sasaki, Y. Monnai, S. Saijo, R. Fujita, H. Watanabe, J. Ishi-Hayase, K. M. Itoh, and E. Abe, Broadband, large-area microwave antenna for optically detected magnetic resonance of nitrogen-vacancy centers in diamond, *Rev. Sci. Instrum.* **87**, 053904 (2016).
- [34] F. C. Ziem, N. S. Götz, A. Zappe, S. Steinert, and J. Wrachtrup, Highly sensitive detection of physiological spins in a microfluidic device, *Nano Lett.* **13**, 4093 (2013).
- [35] S. Nishimura, M. Tsukamoto, K. Sasaki, and K. Kobayashi, Investigations of optical aberration on quantum diamond microscopy toward high spatial resolution and sensitivity, arXiv:2402.14422 [physics.optics].
- [36] F. A. Freire-Moschovitis, R. Rizzato, A. Pershin, M. R. Schepp, R. D. Allert, L. M. Todenhagen, M. S. Brandt, A. Gali, and D. B. Bucher, The Role of Electrolytes in the Relaxation of Near-Surface Spin Defects in Diamond, *ACS Nano* **17**, 10474 (2023).
- [37] P. L. Stanwix, L. M. Pham, J. R. Maze, D. Le Sage, T. K. Yeung, P. Cappellaro, P. R. Hemmer, A. Yacoby, M. D. Lukin, and R. L. Walsworth, Coherence of nitrogen-vacancy electronic spin ensembles in diamond, *Phys. Rev. B* **82**, 201201(R) (2010).
- [38] R. de Sousa, Electron spin as a spectrometer of nuclear spin noise and other fluctuations, arXiv preprint, arXiv:cond-mat/0610716 (2006).
- [39] Y. Ducommun, K. E. Newman, and A. E. Merbach, High-pressure oxygen-17 NMR evidence for a gradual mechanistic changeover from Ia to Id for water exchange on divalent octahedral metal ions going from manganese(II) to nickel(II), *Inorg. Chem.* **19**, 3696 (1980).
- [40] M. Mizuno, T. Iijima, and M. Suhara, Dynamical structure of paramagnetic $[\text{M}(\text{H}_2\text{O})_6][\text{SiF}_6]$ ($\text{M} = \text{Fe}^{2+}, \text{Ni}^{2+}$) crystal studied by means of ^2H nuclear magnetic resonance, *J. Condens. Matter Phys.* **12**, 7261 (2000).
- [41] I. Bertini and C. Luchinat, Chapter 3 relaxation, *Coord. Chem. Rev.* **150**, 77 (1996).
- [42] H. Petzold, P. Djomgoue, G. Hörner, J. M. Speck, T. Ruffer, and D. Schaarschmidt, (^1H) NMR spectroscopic elucidation in solution of the kinetics and thermodynamics of spin crossover for an exceptionally robust $\text{Fe}(2+)$ complex, *Dalton Trans.* **45**, 13798 (2016).
- [43] J.-P. Tetienne, T. Hingant, L. Rondin, A. Cavallès, L. Mayer, G. Dantelle, T. Gacoin, J. Wrachtrup, J.-F. Roch, and V. Jacques, Spin relaxometry of single nitrogen-vacancy defects in diamond nanocrystals for magnetic noise sensing, *Phys. Rev. B* **87**, 235436 (2013).
- [44] Z. Zhang, M. Joos, D. Bluvstein, Y. Lyu, and A. C. Bleszynski Jayich, Reporter-Spin-Assisted T1 Relaxometry, *Phys. Rev. Appl.* **19**, L031004 (2023).
- [45] A. Grosjean, P. Négrier, P. Bordet, C. Etrillard, D. Mondieig, S. Pechev, E. Lebraud, J.-F. Létard, and P. Guionneau, Crystal Structures and Spin Crossover in the Polymeric Material $[\text{Fe}(\text{Htrz})_2(\text{trz})](\text{BF}_4)$ Including Coherent-Domain Size Reduction Effects, *Eur. J. Inorg. Chem.* **2013**, 796 (2013).
- [46] A. Grosjean, N. Daro, B. Kauffmann, A. Kaiba, J.-F. Létard, and P. Guionneau, The 1-D polymeric structure of the $\text{Fe}(\text{NH}_2\text{trz})_3(\text{NO}_3)_2 \cdot n\text{H}_2\text{O}$ (with $n = 2$) spin crossover compound proven by single crystal investigations, *Chem. Commun.* **47**, 12382 (2011).
- [47] J. Wolny, I. Faus, J. Marx, R. Ruffer, A. Chumakov, K. Schlage, H.-C. Wille, and V. Schünemann, Vibrational

Coupling of Nearest Neighbors in 1-D Spin Crossover Polymers of Rigid Bridging Ligands. A Nuclear Inelastic Scattering and DFT Study, *Magnetochemistry* **2**, 19 (2016).

- [48] M. M. Dîrtu, A. Rotaru, D. Gillard, J. Linares, E. Codjovi, B. Tinant, and Y. Garcia, Prediction of the spin transition temperature in Fe(II) one-dimensional coordination polymers: an anion based database, *Inorg. Chem.* **48**, 7838 (2009).
- [49] S. Rackwitz, J. A. Wolny, K. Muffler, K. Achterhold, R. Rüffer, Y. Garcia, R. Diller, and V. Schünemann, Vibrational properties of the polymeric spin crossover (SCO) Fe(II) complexes $[\{\text{Fe}(\text{4-amino-1,2,4-triazole})_3\}\tilde{\text{X}}_2]_n$: a nuclear inelastic scattering (NIS), Raman and DFT study, *Phys. Chem. Chem. Phys.* **14**, 14650 (2012).
- [50] E. Coronado, J. R. Galán-Mascarós, M. Monrabal-Capilla, J. García-Martínez, and P. Pardo-Ibáñez, Bistable Spin-Crossover Nanoparticles Showing Magnetic Thermal Hysteresis near Room Temperature, *Adv. Mater.* **19**, 1359 (2007).

SUPPORTING INFORMATION

A. Estimation of T_1

In our experiments, SCO complexes are brought to proximity with NV centers in diamond. The SCO complexes consist of Fe^{II} ions, which are paramagnetic when in their high-spin (HS) state. This paramagnetic spin bath at the NV center location is characterized by a zero-mean fluctuating magnetic field $\mathbf{B}(t)$, which will influence the NV centers' longitudinal spin relaxation time T_1 . More precisely, the NV centers' longitudinal spin relaxation is influenced by transverse magnetic-field components of the paramagnetic ions with spectral-density amplitude at the NV center transition frequency [S1]. The dynamics of the fluctuating magnetic field caused by molecules or ions with an unpaired electron spin can be described with the correlation function as [S2, S3]

$$\langle B_k(0)B_k(\tau) \rangle = \langle B_k^2 \rangle \exp(-|\tau|/\tau_c). \quad (\text{S1})$$

Here, $\langle B_k^2 \rangle$ ($k = x, y, z$) is the variance of the magnetic field, and the correlation time τ_c of the magnetic field describes the memory of the noise generated by the paramagnetic ions [S2]. The spectral noise density of the magnetic field is given by the Fourier transform of its correlation function, and summarizes the properties of the fluctuating magnetic field. The normalized spectral density is of form [S2, S4]

$$S(\omega) = \frac{2}{\pi} \frac{\tau_c}{1 + \omega^2 \tau_c^2}, \quad (\text{S2})$$

which has the shape of a Lorentzian. In the literature, one finds that τ_c for Fe^{II} lies in the order of 1×10^{-12} s [S5–S8]. From this, we calculate the spectral density of the magnetic field generated by the HS Fe^{II} ions. The calculated normalized spectral noise density for Fe^{II} is shown in the main text in Fig. 2(a). Depending on the quantum sensing scheme, the NV center can detect magnetic noise from sub-Hz over kHz, to MHz, and GHz frequencies [S9]. While, for example, Hahn echoes can be applied to sense noise in the MHz range, T_1 sensing is used to detect noise in the GHz range [S2, S9]. To quantify this, the overlap of the ions' spectral density $S(\omega)$ and the NV-center filter function for T_1 relaxometry $F(\omega)$ is considered of form $\int S(\omega)F(\omega)d\omega$ [S4, S9]. The filter function $F(\omega)$ for T_1 relaxometry is given by

$$F(\omega) = \frac{1}{\pi} \frac{\Gamma}{\Gamma^2 + (\omega - \omega_0)^2}, \quad (\text{S3})$$

where $\Gamma = 1/T_2^*$ is the NV spin dephasing rate and ω_0 is the NV transition frequency [S9]. With the spectral density of the magnetic noise generated by the paramagnetic ions overlapping with the NV centers' spin transition frequency, the NV centers' T_1 time will be reduced due to the ion's fluctuating magnetic field. The NV center's relaxation rate $1/T_1$ under this influence is described by

the relaxation rate $1/T_1'$ of the diamond with intrinsic impurities and an additional rate $1/T_1^{\text{SCO}}$ proportional to spectral density as [S1, S10]

$$\frac{1}{T_1} = \frac{1}{T_1'} + \frac{1}{T_1^{\text{SCO}}}. \quad (\text{S4})$$

Because $1/\tau_c = 1/(1 \times 10^{-12} \text{ s}) \gg \Gamma \approx 1/(50 \times 10^{-9} \text{ s})$, the rate for spin relaxation can be approximated by

$$\frac{1}{T_1} = \frac{1}{T_1'} + A \frac{\gamma_e^2}{2} [S_{B_x}(\omega_0) + S_{B_y}(\omega_0)], \quad (\text{S5})$$

taking into account the transverse components of the magnetic field. The spectral densities of the magnetic-field components are given by [S1, S10]

$$S_{B_{x,y}}(\omega_0) = \int_{-\infty}^{\infty} B_{x,y}(t)B_{x,y}(t+\tau) \exp(-i\omega_0\tau) d\tau. \quad (\text{S6})$$

Here, $A = 3$ is related to the rate equations in an $S = 1$ system [S1], $\gamma_e \approx 2\mu_B/\hbar$ is the gyromagnetic ratio of the electron, μ_B is Bohr's magneton, and \hbar is the reduced Planck constant. Further, $\omega_0 = 2\pi \times 2.87 \text{ GHz}$, is the NV center's spin transition frequency. The integration yields an expression of the transverse magnetic-field variance as [S1, S10]

$$\begin{aligned} \frac{1}{T_1} &= \frac{1}{T_1'} + A \frac{\gamma_e^2}{2} (\langle B_x^2 \rangle + \langle B_y^2 \rangle) \frac{2\tau_c}{1 + \omega_0^2 \tau_c^2} \\ &= \frac{1}{T_1'} + A \gamma_e^2 B_{\perp}^2 \frac{\tau_c}{1 + \omega_0^2 \tau_c^2}. \end{aligned} \quad (\text{S7})$$

Here, B_{\perp}^2 is the variance of the magnetic field perpendicular to the NV quantization axis (z axis). The transverse magnetic-field variance is given by the sum of the magnetic-field variance contributions of each spin i [S1]

$$B_{\perp}^2 = \sum_i B_{\perp,i}^2, \quad (\text{S8})$$

while each magnetic-field variance can be calculated by [S1, S10]

$$B_{\perp,i}^2 = \left(\frac{\mu_0 \gamma_e \hbar}{4\pi} \right)^2 \frac{S(S+1)}{3} \frac{(2 + 3 \sin^2 \alpha_i)}{r_i^6}. \quad (\text{S9})$$

In high spin, the spin quantum number S is $S = 4/2$ for Fe^{II} ions. Further, μ_0 is the vacuum permeability. The angle α_i is the angle between \mathbf{r}_i , which points from the NV center to an Fe^{II} spin, and the NV's quantization axis, see Fig. S1. To estimate the transverse magnetic field components, we microscopically model the influence of the Fe^{II} ions. The Fe^{II} ions in the polymeric SCO complexes are ordered chain-like. To estimate the volume

density of Fe^{II} ions in the SCO samples, we extract the unit-cell volumes of the crystal structure for **SCO I** [S11] and of a crystal structure similar to **SCO II** [S12]. In the case of **SCO I**, a unit cell of volume $V = 1303.2 \text{ \AA}^3$ contains four HS Fe^{II} ions. We calculate the volume density to $\rho_{\text{I}} = 3.1 \times 10^{27} \text{ ions/m}^3$. A unit cell of the structure similar to **SCO II** contains two Fe^{II} ions and is of volume $V = 834.3 \text{ \AA}^3$. Therefore, a volume density ρ_{II} of Fe^{II} ions is given by $\rho_{\text{II}} = 2.4 \times 10^{27} \text{ ions/m}^3$. Assuming a mean angle $\alpha_i(X, Y, Z) \approx \alpha$, we write the transverse magnetic-field variance as

$$B_{\perp}^2 \approx \rho \left(\frac{\mu_0 \gamma_e \hbar}{4\pi} \right)^2 \frac{S(S+1)}{3} (2 + 3 \sin^2 \alpha) \int_d^{\infty} \int_{-\infty}^{\infty} \int_{-\infty}^{\infty} \frac{1}{r^6} dX dY dZ, \quad (\text{S10})$$

with $r = \sqrt{X^2 + Y^2 + Z^2}$ and d the depth of the NV layer in the diamond, yielding

$$B_{\perp}^2 = \rho \left(\frac{\mu_0 \gamma_e \hbar}{4\pi} \right)^2 \frac{S(S+1)}{3} (2 + 3 \sin^2 \alpha) \frac{\pi}{6d^3}. \quad (\text{S11})$$

Since our experiments are performed on a diamond with face orientation (100), we assume $\alpha = 54.75^\circ$ in our calculations. We have verified in numerical simulations that this fixed angle yields similar results to summing all individual contributions with varying distance and angle from an array of Fe^{II} ions as shown in Fig. S1. Importantly, this approximation is only valid for the (100) diamond, as we find discrepancies between the approximate analytical solution and a numerical solution for an NV spin oriented perpendicular to the surface. Using a simulation (“The Stopping and Range of Ions in Matter” (SRIM) [S13]), we determine the mean depth of the NV centers in the diamond to $\bar{d} = 9.3 \text{ nm}$.

It follows that for a distance of the NV centers from the diamond surface of $d = 9.3 \text{ nm}$, the T_1 time of the NV centers will be reduced from $T_1' = 2.80 \text{ ms}$ to $T_1 = 0.18 \text{ ms}$ with HS Fe^{II} ions of **SCO I** and to $T_1 = 0.23 \text{ ms}$ of **SCO II** deposited on the diamond, which are reductions of the relaxation time by one order of magnitude.

B. Confocal setup

Our confocal setup is similar to our widefield setup, see Fig. S2. We use a 520-nm laser of power of $\approx 800 \mu\text{W}$. In the laser beam path, we remove the lens in front of the objective, so that the collimated laser beam enters its aperture. The laser beam is then focused onto the NV-diamond sample. We estimate the laser focus to be $\approx 1 \mu\text{m}$ wide ($1/e^2$ diameter). The NV fluorescence is filtered, and wavelengths $> 665 \text{ nm}$ are detected with two single-photon counting modules (SPCMs). To keep the SPCMs below saturation, we employ neutral-density (ND) filters. For T_1 measurements, we use a sequence that is similar to the one described in our previous work

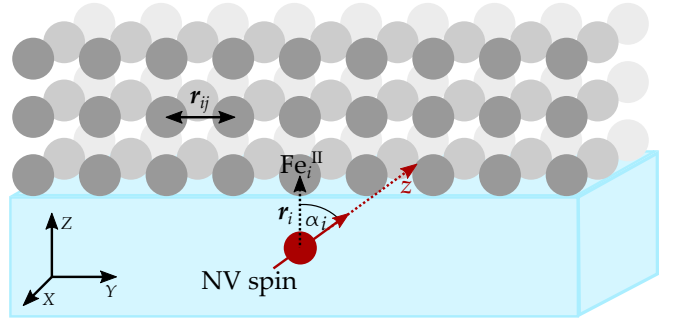


FIG. S1. Schematic drawing of the SCO complexes on the diamond chip. The NV center spin lies at 54.75° to the diamond surface. The vector to a nearby Fe^{II} spin is termed \mathbf{r}_i , and the angle between \mathbf{r}_i and the NV axis is termed α_i . Two Fe^{II} centers are separated by \mathbf{r}_{ij} . The figure was drawn after the description in Ref. [S1]. The NV-quantization axis is marked as the z axis, while the laboratory coordinate system is specified with capital letters.

[S14]. Combined with a time-to-digital converter, we time-resolve the fluorescence during the relaxometry sequence and calculate a T_1 curve, as mentioned in the main text, by forming the mean signal of both SPCMs. We fit the data as described in the main text.

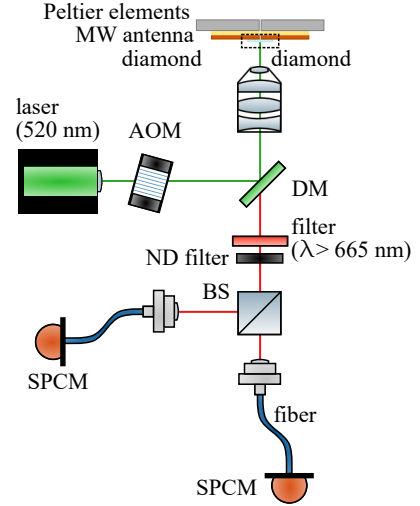


FIG. S2. Confocal configuration of the microscope setup. Compared to the widefield setup, a collimated laser beam enters the objective and is then focused onto the sample. The NV fluorescence $> 665 \text{ nm}$ is detected with single-photon counting modules (SPCMs). Neutral-density (ND) filters are used to keep the SPCMs below saturation.

C. Temperature determination

We heat our sample with Peltier elements and increase the temperature by setting a current. On the surface of the holder, a temperature sensor is mounted. Via

ODMR spectroscopy, we measured the zero-field splitting (ZFS) of the NVs as a function of the temperature we read from our sensor and determined the temperature dependence of the ZFS to $\delta D = -92(1) \text{ kHz K}^{-1}$. All temperature values given in this paper are calculated from a measured resonance or ZFS at the increased temperature with respect to the resonance or ZFS at room temperature. Our temperature sensor determines room temperature to be $19.77(3)^\circ\text{C}$. When mounting the diamond sample in the sample holder, a systematic error arises due to a slightly varying distance of the Peltier elements to the diamond chip. We, therefore, calculate a statistical fit error from Lorentzian fitting to the NV spin resonances in the spectra and determine the temperature by calculating the change in the ZFS. We then combine this error and the difference of our calculated temperature from ODMR spectroscopy to the mean temperature determined by the temperature sensor to the temperature errors in the main text.

D. Temperature dependence of T_1

Since we perform temperature-dependent measurements in our study, we independently investigate the T_1 time as a function of the temperature of the NV-center layer in our diamond chip without an external magnetic field being applied. The experiments were performed as described in the method section in widefield configuration, with 30 accumulated exposures and $N = 1400$ repetitions. As opposed to the evaluation for the SCO-layer samples, we do not evaluate the T_1 curves per pixel since we assume a uniform T_1 time throughout the diamond sample. The mean fluorescence-difference signal as a function of τ is obtained by forming the sum of fluorescence counts of $600 \times 600 \text{ px}^2$ and subtracting the signal with an MW pulse applied from the signal without the MW pulse. We fit a biexponential function to the measurement data described in the main text. The results for T_1 are shown in Fig. S3.

In addition to this study, we performed a similar analysis of the T_1 time with an external magnetic field applied. We note that the T_1 time at room temperature coincides with the T_1 time measured at zero field, and the temperature dependence shows a similar behavior.

E. Raman spectra

We record Raman spectra of the SCO thin layers deposited on the diamond. For **SCO I**, the sample described in the main text was investigated by Raman spectroscopy. In the case of **SCO II**, we noted that the thin layers presented in the main text do not yield reasonable Raman spectra due to insufficient signal intensity. We prepared a slightly thicker layer of **SCO II** using solution 2 and successively drop-cast $20 \mu\text{L}$ onto the diamond chip and remove the solvent (see Methods section). The

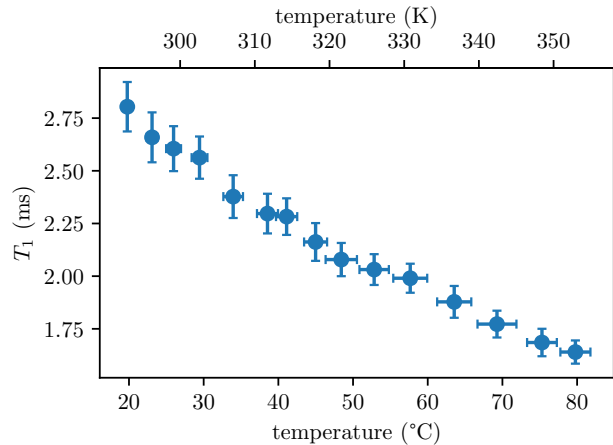


FIG. S3. T_1 of the NVs in the diamond chip as a function of the temperature, recorded with widefield relaxometry.

Raman spectra of **SCO II** below stem from this sample. We expect the thinner layers presented in the main text to have equal spin-transition temperatures. Since the samples of thicker SCO layer detach from the diamond after heating and cooling, they are inaccessible to NV- T_1 measurements in our configuration.

The Raman spectrum of the thin-layer of **SCO I** applied on diamond is depicted in Figs. S4 to S7 at 30°C , 80°C , 110°C , and 85°C , respectively. At 30°C , where the sample is predominantly in the LS state, there are three Raman bands at 134 , 206 , and 280 cm^{-1} . As these bands are not observed in the Raman spectrum at 110°C , we conclude that these bands represent LS marker bands. Accordingly, the bands at 108 , 140 , and 190 cm^{-1} represent HS marker bands. Further marker bands in LS state can be noted at 1057 , 1087 , 1160 , 1280 , 1306 , and 1332 cm^{-1} as well as 805 , 1074 , 1274 , and 1306 cm^{-1} in the HS state. The intense peak at 1332 cm^{-1} is characteristic for the diamond substrate [S15], while the other modes are typical for the thin-layer of the **SCO I** complex [S16]. Based on the spectra, it can be concluded that the sample is predominantly in the LS state at the temperatures used for the determination of the T_1 times.

Furthermore, the Raman spectra of the thin-layer of **SCO II** deposited on diamond at room temperature and at 35°C upon heating are shown in Fig. S8 and Fig. S9. For comparison of the heating and cooling branch of the SCO transition, a further Raman spectrum at room temperature upon cooling from 35°C is displayed in Fig. S10. On the one hand, the Raman spectrum at room temperature in the heating branch shows vibrations at 142 , 180 , 241 , 556 , 695 , 778 , 1040 and 1332 cm^{-1} . On the other hand, the Raman spectrum at 35°C reveals bands at 140 , 180 , 345 , 558 , 691 , 785 , 1040 and 1332 cm^{-1} . The vibration at 1332 cm^{-1} can be attributed to the diamond substrate while all other vibrations are typical for the thin-layer of **SCO II** [S17]. As the vibrations

around 241 cm^{-1} disappear upon heating of the sample, it is concluded that these vibrations are characteristic LS marker bands. Similarly, the vibrations at 140 cm^{-1} and 180 cm^{-1} represent HS marker bands. Therefore, it can be determined that the sample is in a mixed HS and LS state at room temperature and in pure HS state at 35°C . In order to determine the ratio of HS and LS at the different temperatures, the areas under the 180 cm^{-1} and 240 cm^{-1} vibrations were calculated and divided by the sum of both areas. As all three spectra display a noticeable background and noise which are caused by all optical components of the spectrometer, the spectra were corrected using the shape correction tool integrated into the Raman spectrometer. The evaluation of the areas yields 62% HS and 38% at room temperature, 82% HS and 18% LS at 35°C (the LS component occurs due to leftover noise after the shape correction at 240 cm^{-1}) and 84% HS and 16% LS at room temperature upon cooling. Therefore, a considerable difference for the Raman spectra at room temperature can be concluded in dependence of the heating or cooling branch of the hysteresis.

F. Supporting graphs and images

In this section, we plot additional graphs and images. These include LED images of **SCO I** for two subsequent heating and cooling cycles, see Fig. S11. In Fig. S12, we estimate the combined effect of a temperature increase and the presence of paramagnetic SCO complexes on the NV centers' T_1 time for a T_1 map of **SCO II**. Further, additional T_1 maps for measurements on **SCO II** are shown in Figs. S13 and S14. The ΔT_1 maps, which include the statistical fit errors of all T_1 matrices shown in this paper, are displayed in Figs. S15, S16, S17, S18, and S19. In Fig. S20, the ΔT_2 maps are shown. Lastly, a T_2 measurement for the NVs in the clean diamond (no SCO complexes applied) is shown in Fig. S21.

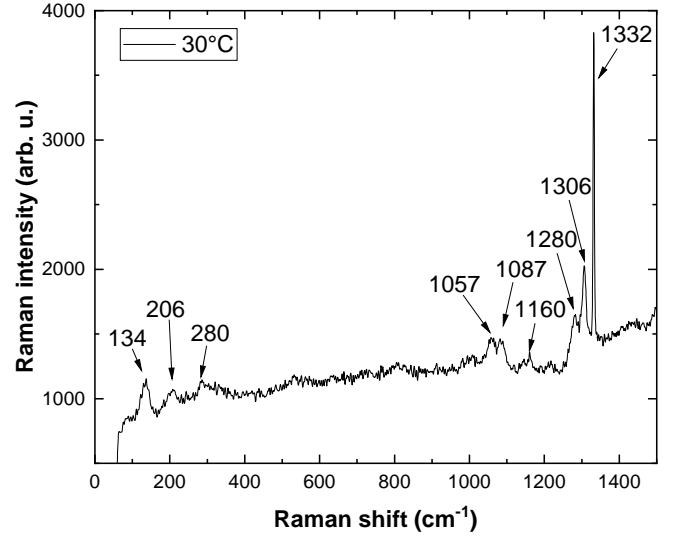


FIG. S4. Raman spectrum for the thin-layer sample of **SCO I** applied on diamond at 30°C .

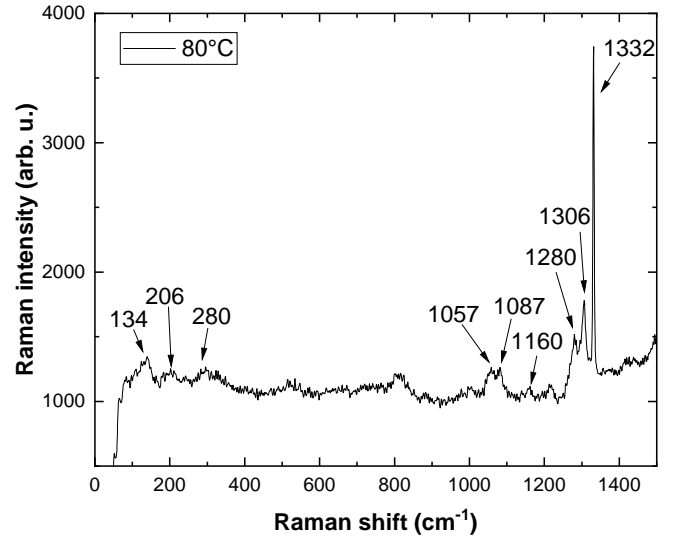


FIG. S5. Raman spectrum for the thin-layer sample of **SCO I** applied on diamond at 80°C in the heating branch.

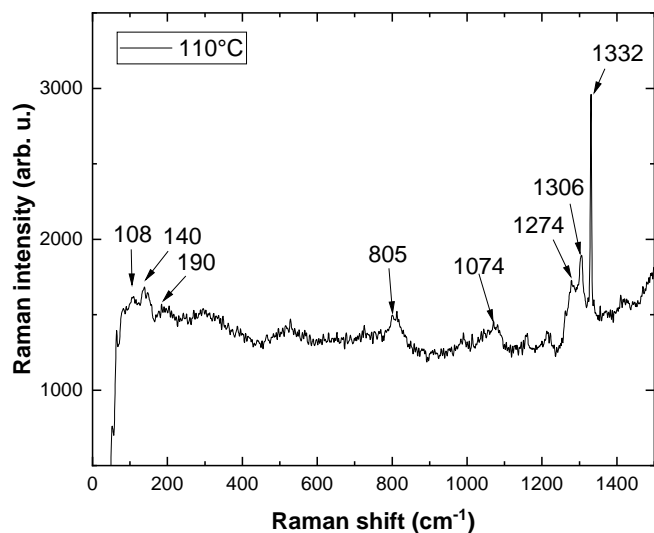
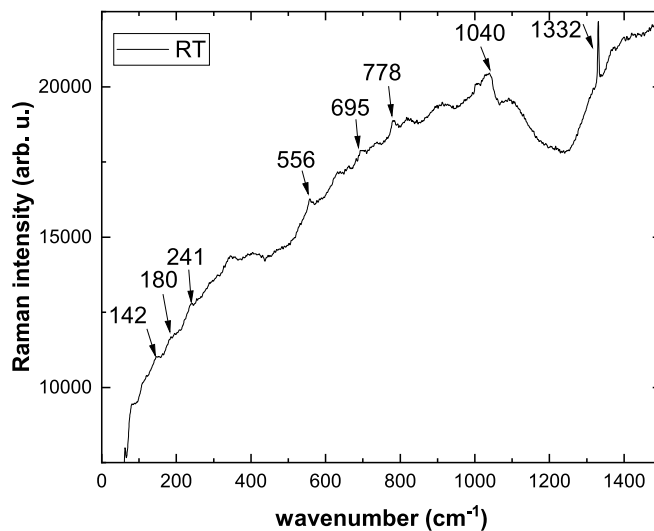


FIG. S6. Raman spectrum for the thin-layer sample of **SCO I** applied on diamond at 110 °C.



Area=1129.35194 Area=693.84774
FWHM=7.58413 FWHM=9.25147

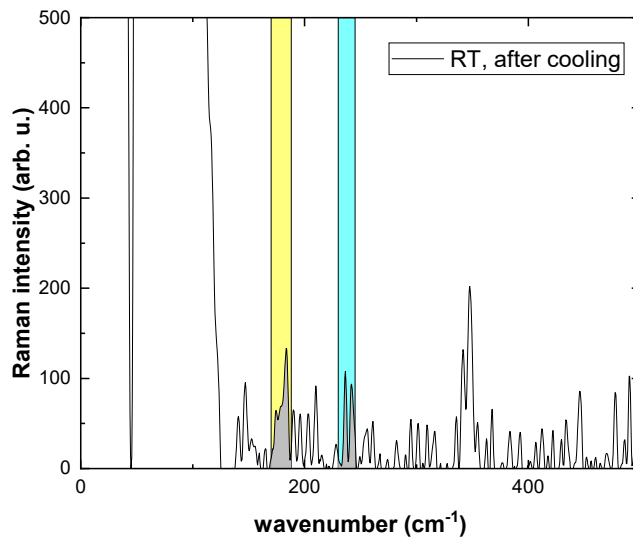


FIG. S8. Full- and background-corrected Raman spectrum for the thin-layer sample of **SCO II** applied on diamond at room temperature in the heating branch.

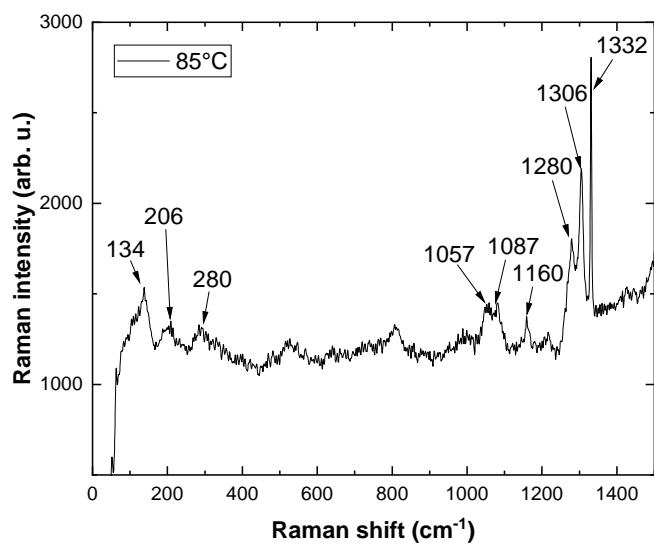


FIG. S7. Raman spectrum for the thin-layer sample of **SCO I** applied on diamond at 85 °C in the cooling branch.

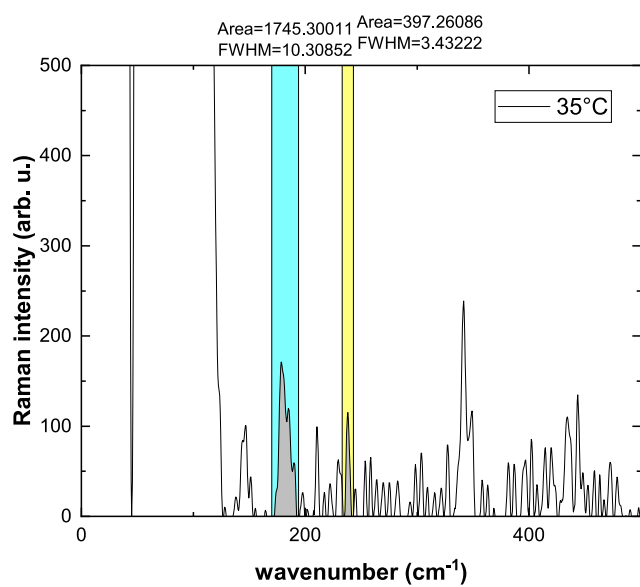
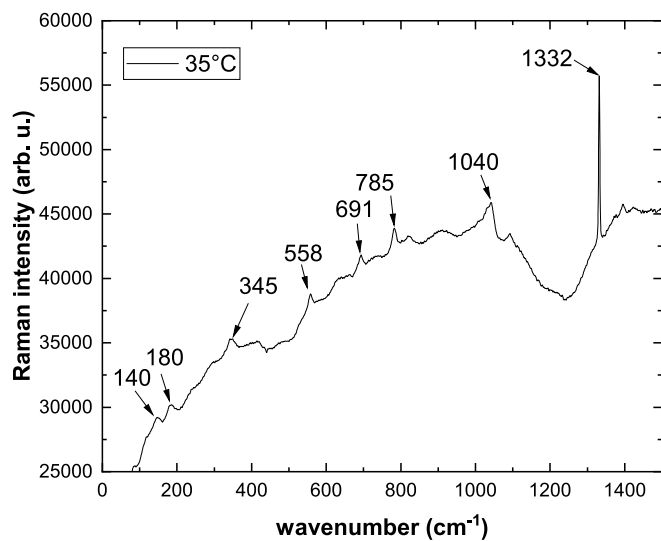


FIG. S9. Full- and background-corrected Raman spectrum for the thin-layer sample of **SCO II** applied on diamond at 35 °C.

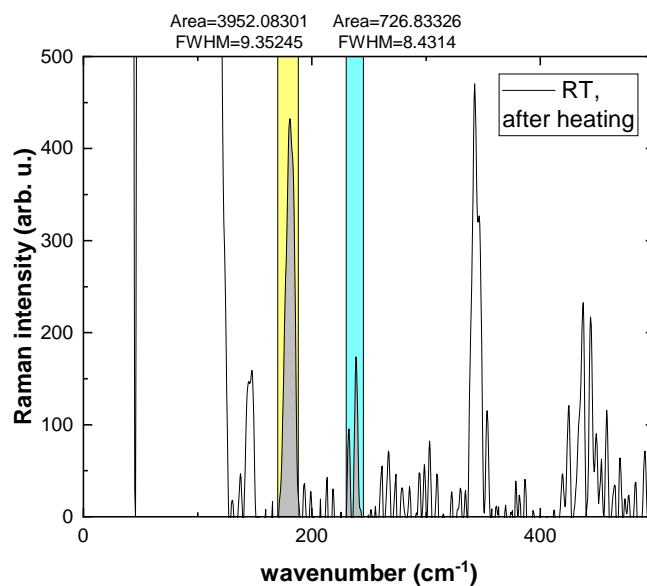


FIG. S10. Raman spectrum for the thin-layer sample of **SCO II** applied on diamond at room temperature in the cooling branch.

- [S1] J.-P. Tetienne, T. Hingant, L. Rondin, A. Cavallès, L. Mayer, G. Dantelle, T. Gacoin, J. Wrachtrup, J.-F. Roch, and V. Jacques, Spin relaxometry of single nitrogen-vacancy defects in diamond nanocrystals for magnetic noise sensing, *Phys. Rev. B* **87**, 235436 (2013).
- [S2] R. de Sousa, Electron spin as a spectrometer of nuclear spin noise and other fluctuations, arXiv preprint, arXiv:cond-mat/0610716 (2006).
- [S3] S. Steinert, F. Ziem, L. T. Hall, A. Zappe, M. Schweikert, N. Götz, A. Aird, G. Balasubramanian, L. Hollenberg, and J. Wrachtrup, Magnetic spin imaging under ambient conditions with sub-cellular resolution, *Nat. Commun.* **4**, 1607 (2013).
- [S4] E. S. Grant, L. T. Hall, L. C. L. Hollenberg, G. McColl, and D. A. Simpson, Nonmonotonic Superparamagnetic Behavior of the Ferritin Iron Core Revealed via Quantum Spin Relaxometry, *ACS Nano* **17**, 372 (2023).
- [S5] Y. Ducommun, K. E. Newman, and A. E. Merbach, High-pressure oxygen-17 NMR evidence for a gradual mechanistic changeover from Ia to Id for water exchange on divalent octahedral metal ions going from manganese(II) to nickel(II), *Inorg. Chem.* **19**, 3696 (1980).
- [S6] M. Mizuno, T. Iijima, and M. Suhara, Dynamical structure of paramagnetic $[M(H_2O)_6][SiF_6]$ ($M = Fe^{2+}, Ni^{2+}$) crystal studied by means of 2H nuclear magnetic resonance, *J. Condens. Matter Phys.* **12**, 7261 (2000).
- [S7] I. Bertini and C. Luchinat, Chapter 3 relaxation, *Coord. Chem. Rev.* **150**, 77 (1996).
- [S8] H. Petzold, P. Djomgoue, G. Hörner, J. M. Speck, T. Rüffer, and D. Schaarschmidt, (1)H NMR spectroscopic elucidation in solution of the kinetics and thermodynamics of spin crossover for an exceptionally robust Fe(2+) complex, *Dalton Trans.* **45**, 13798 (2016).
- [S9] E. Schäfer-Nolte, L. Schlipf, M. Ternes, F. Reinhard, K. Kern, and J. Wrachtrup, Tracking temperature-dependent relaxation times of ferritin nanomagnets with a wideband quantum spectrometer, *Phys. Rev. Lett.* **113**, 217204 (2014).
- [S10] Z. Zhang, M. Joos, D. Bluvstein, Y. Lyu, and A. C. Bleszynski Jayich, Reporter-Spin-Assisted T1 Relaxometry, *Phys. Rev. Appl.* **19**, L031004 (2023).
- [S11] A. Grosjean, P. Négrier, P. Bordet, C. Etrillard, D. Mondieig, S. Pechev, E. Lebraud, J.-F. Létard, and P. Guionneau, Crystal Structures and Spin Crossover in the Polymeric Material $[Fe(Htrz)_2(trz)](BF_4)$ Including Coherent-Domain Size Reduction Effects, *Eur. J. Inorg. Chem.* **2013**, 796 (2013).
- [S12] A. Grosjean, N. Daro, B. Kauffmann, A. Kaiba, J.-F. Létard, and P. Guionneau, The 1-D polymeric structure of the $Fe(NH_2trz)_3(NO_3)_2 \cdot nH_2O$ (with $n = 2$) spin crossover compound proven by single crystal investigations, *Chem. Commun.* **47**, 12382 (2011).
- [S13] J. F. Ziegler, M. D. Ziegler, and J. P. Biersack, SRIM (The Stopping and Range of Ions in Matter), Version SRIM-2013.00 (2012).
- [S14] I. Cardoso Barbosa, J. Gutsche, and A. Widera, Impact of charge conversion on NV-center relaxometry, *Phys. Rev. B* **108**, 075411 (2023).
- [S15] V. S. Gorelik and A. Y. Pyatyshev, Raman scattering in diamond nano- and microcrystals, synthesized at high temperatures and high pressures, *Diam. Relat. Mater.* **110**, 108104 (2020).
- [S16] A. Urakawa, W. van Beek, M. Monrabal-Capilla, J. R. Galán-Mascarós, L. Palin, and M. Milanesio, Combined, Modulation Enhanced X-ray Powder Diffraction and Raman Spectroscopic Study of Structural Transitions in the Spin Crossover Material $[Fe(Htrz)_2(trz)](BF_4)$, *J. Phys. Chem. C* **115**, 1323 (2011).
- [S17] T. Hochdörffer, *Optical and deformation induced spin switching in SCO materials*, *Berichte aus der Physik* (Shaker Verlag, Düren, 2023) ISBN: 978-3-8440-8913-4.

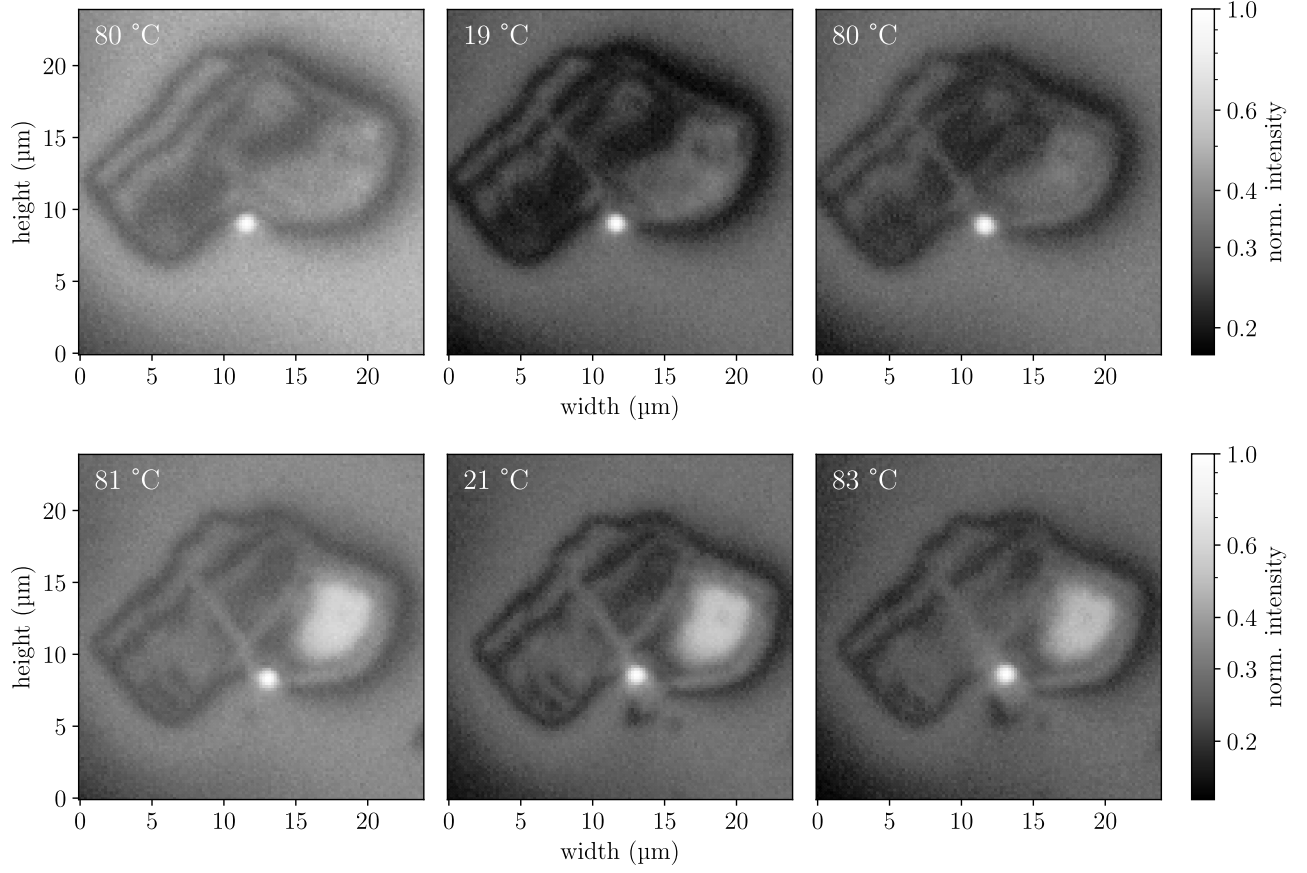


FIG. S11. LED images of the thin-layer sample of **SCO I** for the two subsequent cycles as shown in the main text for the temperatures as given in the images. The images were recorded in their order of appearance at 80(2) °C, 19(1) °C, and 80(2) °C in the first cycle (first row). In the second cycle, the images were recorded at 81(2) °C, 21(1) °C, and 83(1) °C (second row). The exact laser position is marked as a bright spot (filtered NV fluorescence). A structural change in the sample structure is visible, which is most likely caused by the heating and cooling of the sample.

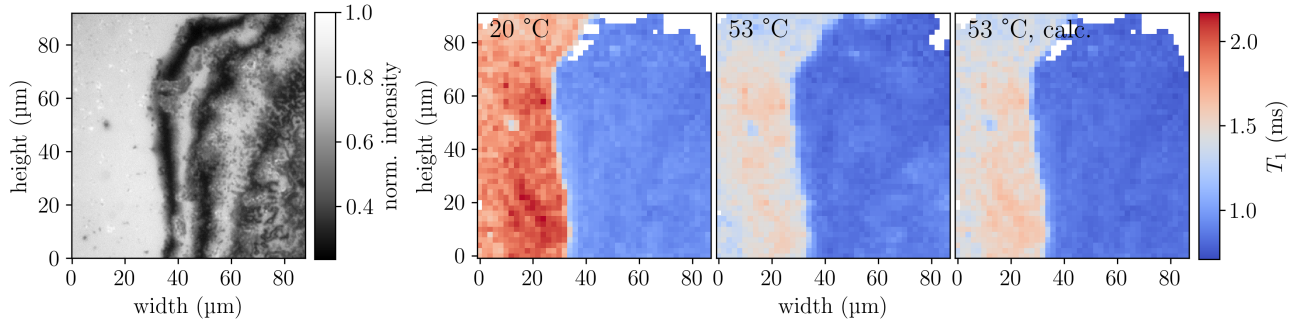


FIG. S12. LED image and T_1 measurements for the thin-layer sample of **SCO II**, sample 1, for different temperatures. The T_1 measurements at 20(1) °C and at 53(2) °C are the same as in Fig. 4. We separate T_1^{SCO} from T_1' at 20 °C using Eq. 3 and add it to T_1' at 53 °C. This way, we obtain the third T_1 map, which describes a calculated T_1 time at 53 °C with the NV- T_1 temperature dependence, but an unchanged SCO influence. Since the difference of the measured and calculated T_1 maps at 53 °C is in the order of the T_1 uncertainties, we exclude influences of an SCO spin switching on the T_1 times.

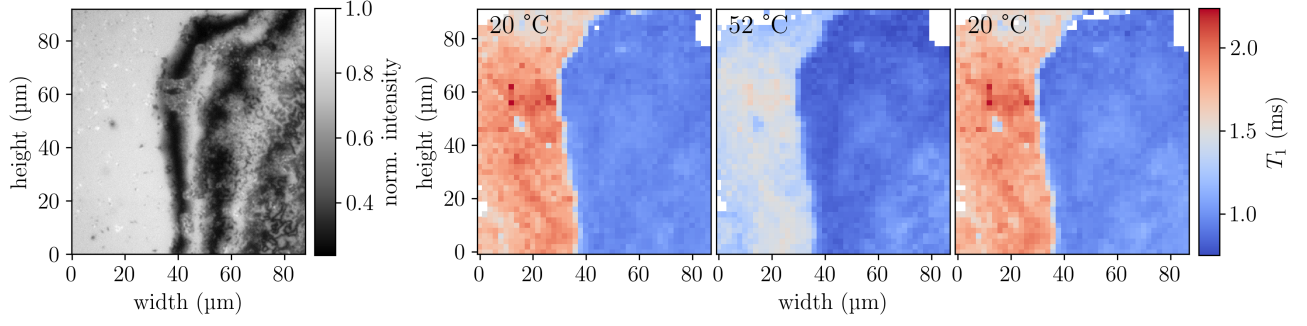


FIG. S13. LED image and T_1 map for the same region at different temperatures for the thin-layer sample 1 of **SCO II**. The results are from a second heating and cooling cycle as presented in the main text, see Fig. 4. The T_1 maps were recorded in order as presented. After cooling the sample to -20°C , we record the T_1 map at $20(1)^\circ\text{C}$ in the heating branch. Then, the T_1 times are measured at $52(2)^\circ\text{C}$. Lastly, the sample is cooled back to $20(1)^\circ\text{C}$ to record the T_1 times in the cooling branch.

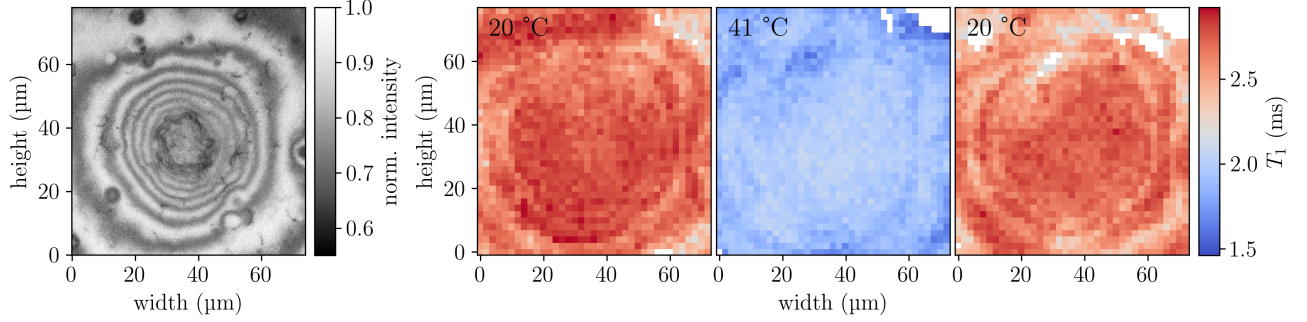


FIG. S14. LED image and T_1 map for the same region at different temperatures for the thin-layer sample 2 of **SCO II**. The results are from the same sample presented in Fig. 5 but at a different position. The T_1 maps were recorded in order as presented. After cooling the sample to -20°C , we record the T_1 map at $20(1)^\circ\text{C}$ in the heating branch. Then, the T_1 times are measured at $41(2)^\circ\text{C}$. Lastly, the sample is cooled back to $20(1)^\circ\text{C}$ to record the T_1 times in the cooling branch.

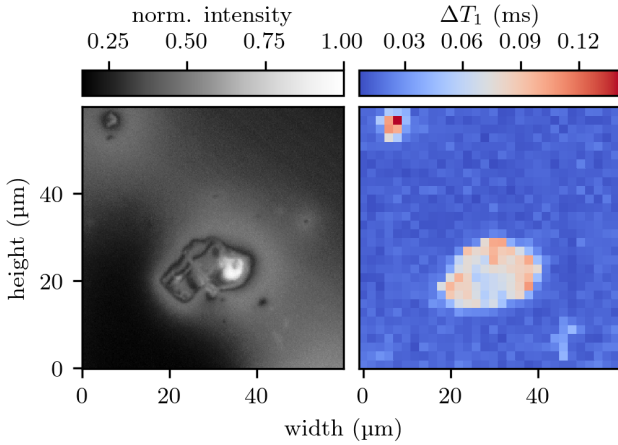


FIG. S15. LED image and values for ΔT_1 of the thin-layer sample of **SCO I**, supporting Fig. 3.

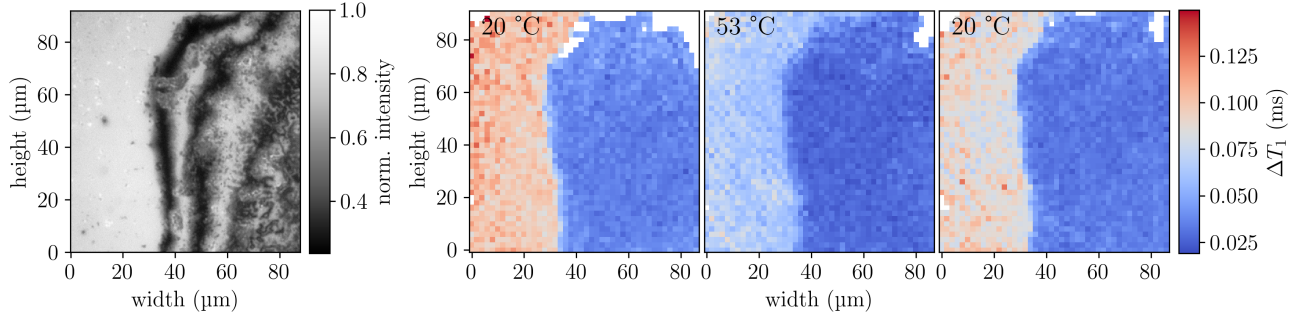


FIG. S16. LED image and values for ΔT_1 for different temperatures of the thin-layer sample 1 of **SCO II** in the first cycle, supporting Fig. 4.

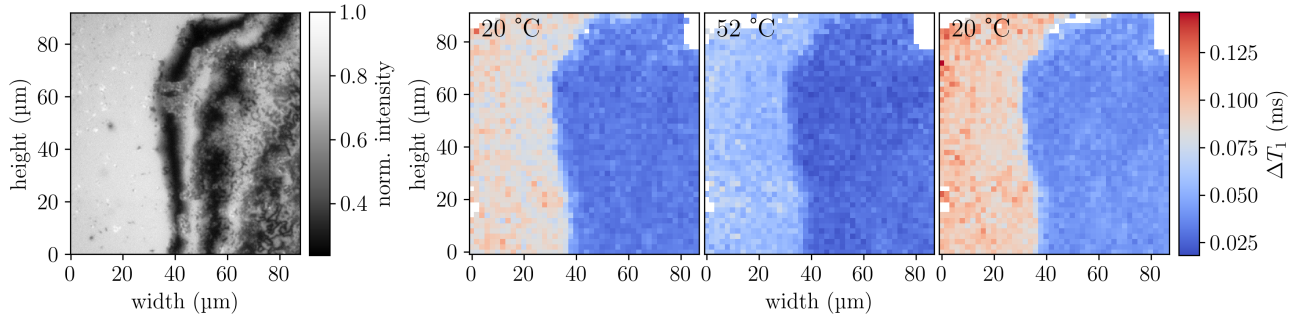


FIG. S17. LED image and values for ΔT_1 for different temperatures of the thin-layer sample 1 of **SCO II** in the second cycle, supporting Fig. S13.

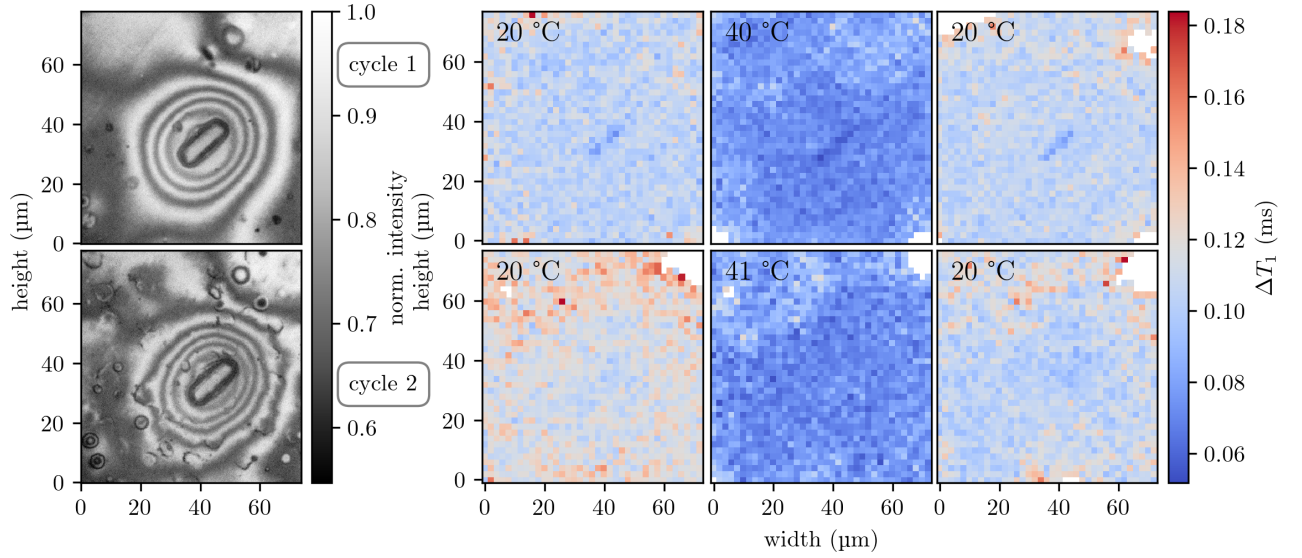


FIG. S18. LED image and values for ΔT_1 for different temperatures of the thin-layer sample 2 of **SCO II** for two subsequent cycles, supporting Fig. 5.

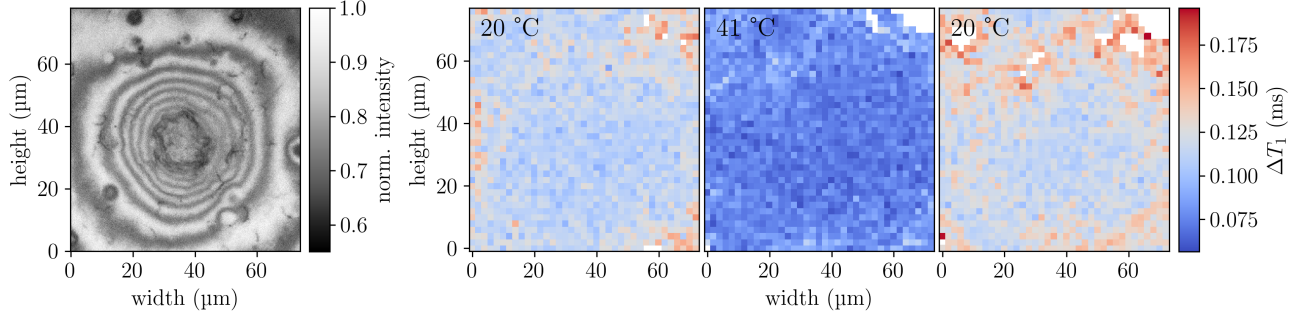


FIG. S19. LED image and values for ΔT_1 for different temperatures of the thin-layer sample 2 of **SCO II** in a second position, supporting Fig. S14.

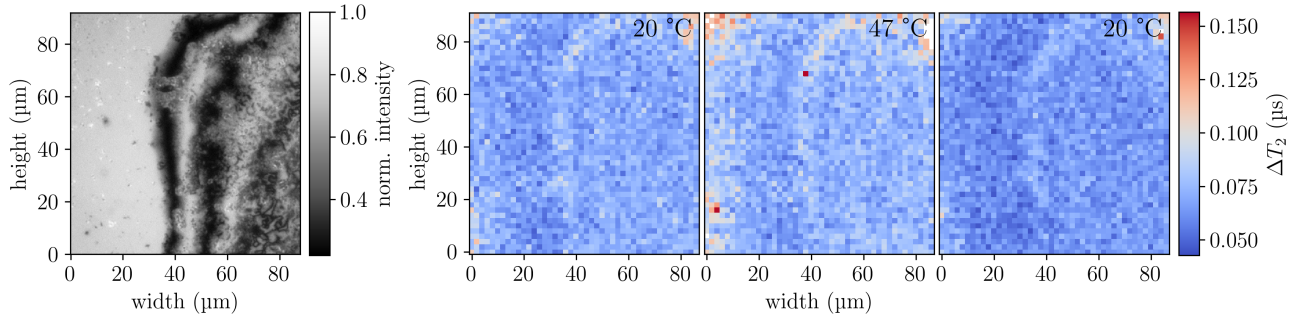


FIG. S20. LED image and values for ΔT_2 for different temperatures of the thin-layer sample 1 of **SCO II**, supporting Fig. 6.

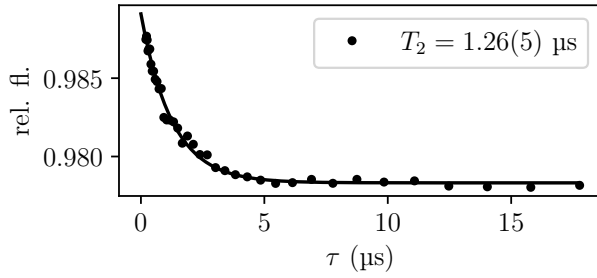


FIG. S21. Results of the T_2 measurement (Hahn echo) of the NV center in the diamond chip without any SCO complexes applied. We measured as described previously. Since we assume the T_2 time to be equal for the entire diamond chip, we do not evaluate the relative fluorescence for each pixel. The relative fluorescence signal as a function of τ is obtained by calculating the sum of fluorescence counts of $600 \times 600 \text{ px}^2$ and forming the quotient of the signal with the MW pulses applied and the signal without the MW pulses. The solid line is a fit curve to the measurement points described in the main text. The data was recorded in an external magnetic field of amplitude in the order of 11 mT. The NV centers of one crystal orientation were probed at $\approx 2817 \text{ MHz}$.